6-21-2022

Mitochondrial cyclophilin D promotes disease tolerance by licensing NK cell development and IL-22 production against influenza virus

Jeffrey Downey
McGill University

Haley E Randolph
University of Chicago

Erwan Pernet
McGill University

Kim A Tran
McGill University

Shabaana A Khader
Washington University School of Medicine in St. Louis

See next page for additional authors

Cell Reports

Article

Mitochondrial cyclophilin D promotes disease tolerance by licensing NK cell development and IL-22 production against influenza virus

Graphical abstract

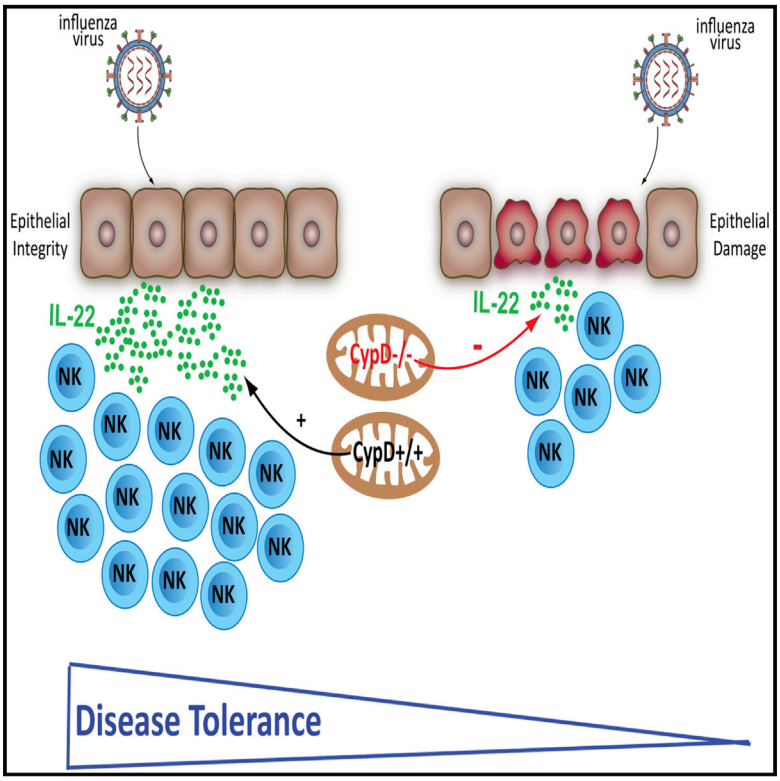

Authors

Jeffrey Downey, Haley E. Randolph, Erwan Pernet, ..., Irah L. King, Luis B. Barreiro, Maziar Divangahi

Correspondence

maziar.divangahi@mcgill.ca

In brief

Downey et al. show that CypD is critical in immunity to influenza A virus (IAV) infection by promoting disease tolerance. CypD regulates NK cell hematopoiesis in the bone marrow and the accumulation of mature IL-22-producing NK cells in the airways, which protect the pulmonary epithelium from IAV-induced damage.

Highlights

- Mitochondrial CypD is required to protect against severe influenza infection
- CypD expression promotes NK cell lymphopoiesis and maturation
- NK cell-derived IL-22 enhances disease tolerance during influenza infection
- Transfer of WT NK cells confers protection in *CypD*$^{-/-}$ mice to influenza infection

Downey et al., 2022, Cell Reports *39*, 110974
June 21, 2022
https://doi.org/10.1016/j.celrep.2022.110974

CellPress

Cell Reports

CellPress
OPEN ACCESS

Article

Mitochondrial cyclophilin D promotes disease tolerance by licensing NK cell development and IL-22 production against influenza virus

Jeffrey Downey,[1,2,3] Haley E. Randolph,[4] Erwan Pernet,[1,2,3] Kim A. Tran,[1,2,3] Shabaana A. Khader,[5,6] Irah L. King,[1,2,3] Luis B. Barreiro,[4,7] and Maziar Divangahi[1,2,3,8,*]

[1]Department of Medicine, McGill University Health Centre, McGill International TB Centre, Meakins-Christie Laboratories, McGill University, 1001 Decarie Boulevard, Montreal, QC H4A 3J1, Canada
[2]Department of Pathology, McGill University Health Centre, McGill International TB Centre, Meakins-Christie Laboratories, McGill University, 1001 Decarie Boulevard, Montreal, QC H4A 3J1, Canada
[3]Department of Microbiology & Immunology, McGill University Health Centre, McGill International TB Centre, Meakins-Christie Laboratories, McGill University, 1001 Decarie Boulevard, Montreal, QC H4A 3J1, Canada
[4]Genetics, Genomics, and Systems Biology, University of Chicago, Chicago, IL, USA
[5]Department of Pathology and Immunology, Washington University School of Medicine, St. Louis, MO, USA
[6]Department of Molecular Microbiology, Washington University School of Medicine, St. Louis, MO, USA
[7]Section of Genetic Medicine, Department of Medicine, University of Chicago, Chicago, IL, USA
[8]Lead contact
*Correspondence: maziar.divangahi@mcgill.ca
https://doi.org/10.1016/j.celrep.2022.110974

SUMMARY

Severity of pulmonary viral infections, including influenza A virus (IAV), is linked to excessive immunopathology, which impairs lung function. Thus, the same immune responses that limit viral replication can concomitantly cause lung damage that must be countered by largely uncharacterized disease tolerance mechanisms. Here, we show that mitochondrial cyclophilin D (CypD) protects against IAV via disease tolerance. *CypD*$^{-/-}$ mice are significantly more susceptible to IAV infection despite comparable antiviral immunity. This susceptibility results from damage to the lung epithelial barrier caused by a reduction in interleukin-22 (IL-22)-producing natural killer (NK) cells. Transcriptomic and functional data reveal that *CypD*$^{-/-}$ NK cells are immature and have altered cellular metabolism and impaired IL-22 production, correlating with dysregulated bone marrow lymphopoiesis. Administration of recombinant IL-22 or transfer of wild-type (WT) NK cells abrogates pulmonary damage and protects *CypD*$^{-/-}$ mice after IAV infection. Collectively, these results demonstrate a key role for CypD in NK cell-mediated disease tolerance.

INTRODUCTION

In response to any given infection, host resistance is involved in preventing pathogen invasion or replication. These resistance mechanisms are a critical component of host defense to infection, yet they come with a considerable inflammatory cost that paradoxically threatens host fitness through excessive immunopathology. Thus, mechanisms of disease tolerance are required to mitigate tissue damage, restore organ function, and counter the cost of anti-microbial inflammation (Martins et al., 2019; Medzhitov et al., 2012; Meunier et al., 2017; Schneider and Ayres, 2008). Severe and fatal influenza A virus (IAV) infections are more often triggered by a "cytokine storm" that contributes to a break in disease tolerance, rather than ineffective host resistance (Bautista et al., 2010; Brandes et al., 2013; Perrone et al., 2008). On the other hand, 16% of IAV infections are estimated to be asymptomatic (Leung et al., 2015), suggesting that, in certain individuals, tolerance mechanisms sufficiently avoid disease. Thus, understanding disease tolerance during respiratory infection may uncover targetable pathways for novel immunotherapies.

IAV infections are short-lived and usually self-resolving within 7–10 days, though inflammation can persist for weeks after infection. The early inflammatory response is marked by an influx of innate leukocytes into the infected lung and airways. While inflammatory monocyte-derived cells play important roles in host resistance and priming of the adaptive immune response (Aldridge et al., 2009; Lin et al., 2008; Narasaraju et al., 2011), they can jeopardize host survival by causing substantial collateral immunopathology (Dawson et al., 2000; Herold et al., 2008). Mechanistically, our group highlighted the importance of the bioactive lipid leukotriene B_4 (LTB_4) in inhibiting *in situ* proliferation of inflammatory monocyte-derived macrophages (IMM) to conserve pulmonary epithelial integrity (Pernet et al., 2019). Equally, reduction of extracellular matrix (ECM) turnover during IAV infection protects mice by conserving epithelial structure (Talmi-Frank et al., 2016). Therefore, maintenance of the lung architecture and physiology is an essential component of host defense.

In addition to myeloid cells, innate lymphoid cells (ILCs), such as natural killer (NK) cells, accumulate in the lung as early as

2 days post-infection (Carlin et al., 2018). NK cells express a variety of activating and inhibitory receptors that perform diverse context- and tissue-specific functions, including well-described roles in the killing of virally infected cells in a non-major histocompatibility complex (MHC)-restricted manner (Vivier et al., 2008). In the context of IAV infection, NK cells contribute to host resistance by recognizing sialylated hemagglutinin (HA) proteins (Glasner et al., 2012; Mandelboim et al., 2001) on the surface of IAV-infected cells to facilitate lysis (Gazit et al., 2006; Li et al., 2017; Stein-Streilein and Guffee, 1986). Beyond their cytotoxic role in host resistance, NK cells are equally critical in disease tolerance by secreting the epithelium-protective cytokine interleukin-22 (IL-22) (McAleer and Kolls, 2014). IL-22 maintains mucosal barriers by inducing survival and proliferation of epithelial cells. Although several cell types can produce IL-22 (Ivanov et al., 2013; Paget et al., 2012), conventional NK cells have been suggested to be the major source following IAV infection (Guo and Topham, 2010). Consistently, *Il22*$^{-/-}$ mice exhibit enhanced epithelial damage and pulmonary pathology in response to IAV (Ivanov et al., 2013; Kumar et al., 2013; Pociask et al., 2013). However, our understanding of the mechanisms involved in the production of IL-22 by NK cells in this setting is incomplete.

Mitochondrial cyclophilin D (CypD), encoded by the *Peptidyl-prolyl isomerase F* (*Ppif*) gene, is a member of the cyclophilin family of isomerases that resides within the mitochondrial matrix. CypD is an essential modulator of the mitochondrial permeability transition pore (MPTP), which is required for the induction of necrosis (Baines et al., 2005; Nakagawa et al., 2005; Zhao et al., 2017). Given the regulatory role of CypD in necrosis (Nakagawa et al., 2005; Zhao et al., 2017) and the importance of conserved macrophage viability following infection (Downey et al., 2018; Ghoneim et al., 2013; Jaworska et al., 2014), we initially hypothesized that the loss of CypD-mediated necrosis would enhance macrophage viability and protect against IAV. In fact, *CypD*$^{-/-}$ mice were highly susceptible to IAV infection without alteration in necrosis or host resistance. RNA sequencing (RNA-seq) of purified NK cells revealed an altered transcriptome in *CypD*$^{-/-}$ cells, marked by an immature profile (Chiossone et al., 2009) that affected their metabolism (O'Brien and Finlay, 2019) and function. Studies in the bone marrow revealed that CypD promotes NK cell hematopoiesis by preventing the death of NK cell progenitors, while in the periphery, a lack of IL-22 production by NK cells in the infected airways was the major cause of susceptibility of *CypD*$^{-/-}$ mice. Collectively, our findings highlight an important role for CypD in NK cell-mediated disease tolerance to IAV infection.

RESULTS

CypD is required for disease tolerance during IAV infection

Given the requirement of CypD in necrosis (Baines et al., 2005; Nakagawa et al., 2005) and the relationship between IAV pathogenesis and cell death (Downey et al., 2018), we postulated that *CypD*$^{-/-}$ mice are more protected to IAV. We infected wild-type (WT) and *CypD*$^{-/-}$ mice with a lethal dose (~LD_{50}) (90 plaque-forming units [PFUs]) of PR8 IAV. At this dose, *CypD*$^{-/-}$ mice were highly susceptible to IAV infection, exhibiting increased mortality (Figure 1A) and morbidity (Figure 1B). To investigate this susceptibility, we used a 50 PFU dose that was sublethal in all mice. The enhanced susceptibility of *CypD*$^{-/-}$ mice was not due to differences in pulmonary necrosis, as determined by lactate dehydrogenase (LDH) levels in the bronchoalveolar lavage (BAL) (Figure S1A), or host resistance, as pulmonary viral loads (Figure 1C) and type I interferon (IFN-I) were similar between WT and *CypD*$^{-/-}$ mice (Figures 1D, 1E, S1B, and S1C). We next hypothesized that this susceptibility was linked to impaired disease tolerance. At day 7 post-infection, *CypD*$^{-/-}$ mice exhibited enhanced pulmonary edema (Figure 1F) and barrier damage, as shown by elevated protein and erythrocytes in the BAL (Figures 1G, 1H, and S1D), due to a significant increase in epithelial and endothelial damage of *CypD*$^{-/-}$ mice (Figure 1I). Both flow cytometry and H&E staining showed that this increased pulmonary damage was associated with elevated inflammatory cells in the parenchyma and airways of *CypD*$^{-/-}$ lungs (Figures 1J–1L), while Masson's trichrome stain revealed enhanced collagen deposition (Figures 1M and 1N). To rule out the potential impact of genetic background or microbiome confounders, we performed experiments in littermates and recapitulated our findings (Figures S1E–S1H). Taken together, these data show that CypD aids in immunity to IAV by regulating disease tolerance, rather than host resistance.

Immune, not stromal, cells are responsible for the susceptibility of *CypD*$^{-/-}$ mice to IAV

Mechanisms of disease tolerance can be mediated by structural or hematopoietic compartments (Medzhitov et al., 2012; Schneider and Ayres, 2008; Soares et al., 2017). To delineate which was primarily responsible for the increased tissue damage in *CypD*$^{-/-}$ mice, we generated bone marrow (BM) chimeric mice, where the hematopoietic compartment of lethally irradiated CD45.1 WT mice was reconstituted with *CypD*$^{-/-}$ cells (CD45.2) (*CypD*$^{-/-}$ → WT) BM and vice versa (WT → *CypD*$^{-/-}$). After 12 weeks, reconstitution efficiency was greater than 92% (Figure S2A). For further analysis, we chose day 7 post-IAV infection to match the peak of lung damage (Figure 1). *CypD*$^{-/-}$ → WT mice showed a statistically significant increase in erythrocytes in the BAL with enhanced pulmonary inflammation and collagen deposition when compared with WT (Figures 2A–2D and S2B), whilethere was only a modest, non-significant increase in WT → *CypD*$^{-/-}$ mice. Thus, the reduced disease tolerance in *CypD*$^{-/-}$ mice is predominately mediated by the hematopoietic compartment.

To elucidate which immune cell is responsible for this susceptibility, we phenotyped innate immune cells by flow cytometry post-IAV infection (gating strategy Figures S1I and S1J). We and others have previously shown that IMM, neutrophils and pro-inflammatory monocytes can compromise disease tolerance during IAV infection (Narasaraju et al., 2011; Pernet et al., 2019). However, the kinetics of IMM, neutrophils, and Ly6C^{hi} monocytes in the BAL showed no significant differences in either frequencies or numbers between groups (Figures 2E, 2F, and S2C). Instead, we found that the kinetics of NK cell accumulation in the airways differed, with a significant reduction in the frequency of NK cells at day 7 post-IAV infection in *CypD*$^{-/-}$ mice compared to littermate control mice (Figures 2G and S2D). No differences were observed in the parenchymal immune cells (Figures S2E–S2H).

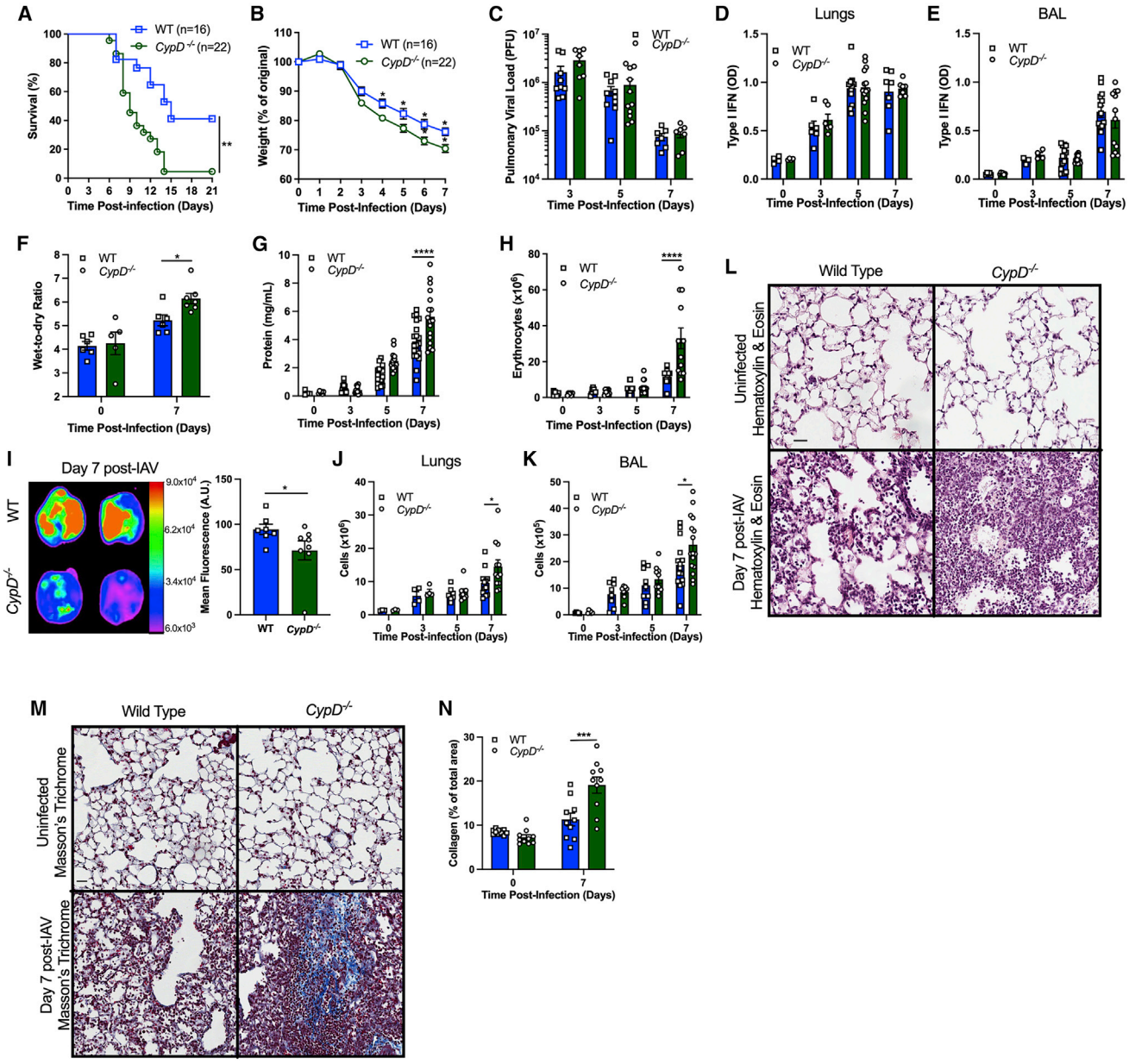

Figure 1. CypD protects against IAV infection by promoting disease tolerance

(A and B) Mice were infected with 90 plaque-forming units (PFU) of influenza A virus (IAV). Survival (A) and weight loss (B) were monitored.

(C–N) Mice were infected with 50 PFU. Viral load (C) and total active type I interferon (IFN-I) in the lungs (D) or bronchoalveolar lavage (BAL) (E) were measured. Lung wet-to-dry ratio (F) and protein (G) or erythrocytes (H) in the BAL are shown. (I) Fluorescence intensity of lungs following Texas Red Dextran administration was assessed. Total cell counts in the lungs (J) and BAL (K) were quantified by flow cytometry. Micrographs of lungs stained with H&E (L; scale bar represents 30 μM) or Masson's trichrome (M; scale bar represents 20 μM) are shown, as quantified in (N).

In (A) and (B), total mice are denoted in the figures; in (C)–(K), each symbol is a unique mouse; in (L) and (M), micrographs are representative of five mice; and in (N), each symbol is one random micrograph (n = 10 micrographs total). All are a compilation of at least two experiments. Statistical analyses are log rank test (A), two-way ANOVA followed by Sidak's multiple comparison test (B–H, J, K, and N), or two-tailed Student's t test (I). *p<0.05, **p<0.01, ***p<0.001, ****p<0.0001. See also Figure S1.

CypD$^{-/-}$ NK cells are phenotypically immature

NK cells are required for protection against IAV by regulating both host resistance and disease tolerance (Gazit et al., 2006; Kumar et al., 2013; Sengupta et al., 2019). NKp46/IAV HA interactions elicit cell lysis via perforin and granzyme to kill virally infected cells (Gazit et al., 2006; Mandelboim et al., 2001). However, *CypD*$^{-/-}$ and WT NK cells expressed similar levels of perforin and granzyme B (Figure 2H), suggesting no difference in their cytotoxicity. The maturation of NK cells is known to be dependent on the downregulation of CD27 and upregulation of CD11b, which gives

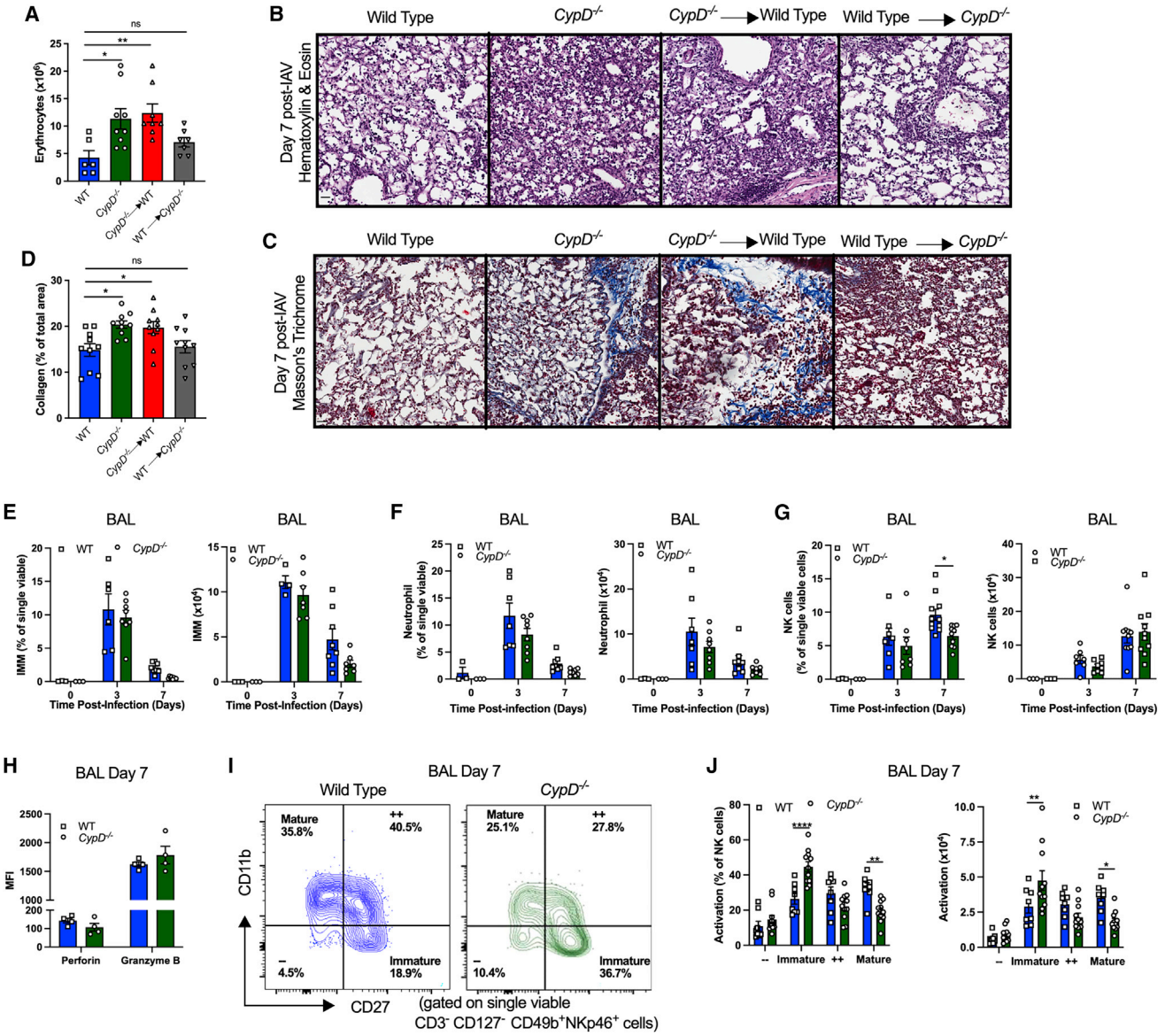

Figure 2. Intrinsic function of CypD in hematopoietic progenitor cells is required for NK cell maturation

(A–J) Mice were infected with 50 PFU.

(A–D) Chimeric mice were generated by reconstituting irradiated *CypD*$^{-/-}$ mice (CD45.2) with CD45.1 bone marrow (WT → *CypD*$^{-/-}$) or irradiated CD45.1 mice with *CypD*$^{-/-}$ bone marrow (*CypD*$^{-/-}$ → WT). Erythrocytes in the BAL were enumerated (A). Micrographs of H&E-stained lungs (B; scale bar represents 30 μM) or Masson's trichrome (C; scale bar represents 30 μM) are shown, as quantified in (D).

(E–G) Total frequencies (left panels) and cell counts (right panels) of IMM (E), neutrophils (F), and NK cells (G) in the BAL.

(H) Mean fluorescence intensity (MFI) of perforin or granzyme B within NK cells.

(I) Representative flow plots of CD27 and CD11b expression on NK cells in the BAL.

(J) Percentages (left panel) and total cells counts (right panel) of NK cell subsets in the BAL.

Each symbol indicates a separate mouse, except in (B) and (C), which is a representative figure of four; (D), where each symbol is one quantified micrograph of 10; and (I), which is a representative plot compiled in (J). All are a compilation of at least two experiments, except for (H), which is one representative of two. Statistical analyses are one-way ANOVA followed by Tukey's multiple comparisons (A and D), two-way ANOVA followed by Sidak's multiple comparison test (E–G and J), or two-tailed Student's t test (H). ns, not significant; *p<0.05, **p<0.01, ***p<0.001, ****p<0.0001. See also Figure S2.

rise to distinct populations of NK cells (CD27^{-} CD11b^{-}, CD27^{+} CD11b^{-}, CD27^{+} CD11b^{+}, and CD27^{-} CD11b^{+}) (Chiossone et al., 2009; Collin et al., 2017; Fu et al., 2011). Single-cell analysis has confirmed differences in effector function of these NK cell populations (Crinier et al., 2018). Intriguingly, NK cells from *CypD*$^{-/-}$ mice exhibited elevated immature (CD27^{+} CD11b^{-}) cells compared to fully mature (CD27^{-} CD11b^{+}) cells in the BAL (Figures 2I, 2J, and S2I), but not in the lung (Figures S2J and

S2K) at day 7 post-IAV infection. Similar results were obtained in splenic NK cells at day 5 post-IAV infection (Figure S2L). Thus, at the peak of IAV-induced damage, *CypD*$^{-/-}$ mice have reduced mature NK cells.

CypD$^{-/-}$ NK cells have an altered transcriptional profile and metabolic program

As NK cell dynamics differed between WT and *CypD*$^{-/-}$ mice following IAV infection, we next asked whether *CypD* is expressed within them. We purified NK cells from WT and *CypD*$^{-/-}$ spleens and found significant expression of *CypD* and mitochondria-localized CYPD protein in WT, but not *CypD*$^{-/-}$, NK cells (Figures S3A and S3B). We then performed bulk RNA-seq on WT and *CypD*$^{-/-}$ splenic NK cells isolated at day 5 post-IAV infection (Table S1), as at this time point post IAV infection the maturation state of splenic NK cells matched with the those in the BAL at day 7 post-infection. Principal-component analysis (PCA) on splenic WT and *CypD*$^{-/-}$ NK cell expression data revealed a strong signature of IAV infection, with non-infected and IAV-infected samples separating on PC1, which explained 56.3% of the variance (Figure S3C). Within IAV-infected samples, we found 315 genes for which expression patterns significantly differed (|logFC| > 0.5; false discovery rate [FDR] < 0.10) between WT and *CypD*$^{-/-}$ NK cells (Figure 3A; Table S2), including *Ppif*. Gene ontology (GO) enrichment analysis revealed that genes showing significantly higher expression in WT NK cells (n = 146) were enriched for activation of the immune response (FDR = 4.3×10^{-4}), phagocytosis (FDR = 5.3×10^{-5}), wound healing (FDR = 4.1×10^{-4}), and blood coagulation (FDR = 5.3×10^{-4}) (Figure 3B; Table S3), while genes more highly expressed in *CypD*$^{-/-}$ NK cells (n = 169) were enriched for oxidative phosphorylation (OXPHOS) (FDR = 2.5×10^{-3}), T-cell-mediated toxicity (FDR = 3.2×10^{-3}), porphyrin-containing compound metabolic processes (FDR = 5.1×10^{-3}), and peroxidase activity (FDR = 1.5×10^{-4}) (Figure 3C; Table S3). In line with splenic *CypD*$^{-/-}$ NK cells displaying significantly more immature and fewer fully mature NK cells, we found that genes previously associated with elevated expression in fully mature and intermediate-mature NK cells (Chiossone et al., 2009) were significantly enriched for higher expression in WT mice (Figure S3D).

Gene set enrichment analysis (GSEA) using the Molecular Signatures Database hallmark gene sets (Liberzon et al., 2015) highlighted a divergence in multiple metabolic and signaling pathways, including an enrichment for Wnt/β-catenin in WT NK cells (FDR = 0.024) (Figure 3E; Table S3) and enrichments for mTORC1 signaling (FDR = 3.3×10^{-4}) and OXPHOS (FDR = 1.7×10^{-4}) in *CypD*$^{-/-}$ NK cells (Figures 3F and 3G; Table S3). Concordantly, the average expression of genes belonging to the Wnt/β-catenin signaling pathway was significantly higher in WT NK cells (Figure 3H; t test; p = 4.2×10^{-3}), while the OXPHOS and mTORC1 signaling pathways elicited a trend toward higher expression in the *CypD*$^{-/-}$ NK cells (Figures S3E and S3F; t test; p = 0.06 and p = 0.24, respectively).

The Wnt/β-catenin signaling pathway has been shown to be critical in the progression to mature CD11b^{+} NK cells (Zhang et al., 2009), while OXPHOS and mTORC1 signaling is associated with an immature state (Marçais et al., 2014; O'Brien and Finlay, 2019; Yang et al., 2018). CypD is equally known to regulate ATP synthase and OXPHOS (Porter and Beutner, 2018). To see whether enhanced OXPHOS enrichment led to elevated mitochondrial respiration in *CypD*$^{-/-}$ NK cells, we subjected them to the Seahorse assay. At steady state, we detected no differences in OXPHOS between WT and *CypD*$^{-/-}$ NK cells (Figures S3G–S3J). However, following IAV infection, we observed a significant increase in basal metabolic rate, maximal respiration, and spare respiratory capacity in *CypD*$^{-/-}$ NK cells compared with WT (Figures 3I–3P). We also found an increase in healthy respiring and disrupted mitochondria in *CypD*$^{-/-}$ NK cells at day 3 post-IAV infection (Figures 3Q–3S), as well as mitochondrial reactive oxygen species (ROS) production (Figure 3T), suggesting mitochondrial dysfunction. Taken together, RNA-seq, flow cytometry, and functional data indicate that CypD regulates NK cell maturation and metabolism.

CypD expression in NK cells promotes transcriptional pathways involved in wound healing

We next sought to dissect the transcriptional differences in functional immune-related pathways between WT and *CypD*$^{-/-}$ NK cells. Numerous killer cell lectin-like receptor genes (*Klr*) were differentially expressed between NK cells of WT and *CypD*$^{-/-}$ mice post-IAV infection (Figure 3A), including *Klri2*, *Klr8*, *Klra17*, and *Klra5*, suggesting alteration in their functional capabilities. Indeed, the transcriptional immune response signatures of WT and *CypD*$^{-/-}$ NK cells were distinct after IAV infection. *CypD*$^{-/-}$ NK cells were enriched for higher expression of antigen processing (FDR = 7.8×10^{-3}) and T-cell-mediated cytotoxicity (FDR = 3.2×10^{-3}) pathways (Figure 4A; Table S3), whereas WT NK cells were enriched for phagocytosis and engulfment (FDR = 1.1×10^{-3}) and complement-dependent cytotoxicity (FDR = 8.0×10^{-4}) (Figure 4B; Table S3). Notably in WT NK cells, we also identified significant enrichments for pathways involved in cytokine secretion, including IL-10 production (FDR = 5.6×10^{-3}), negative regulation of IL-13 secretion (FDR = 6.8×10^{-4}), and chemokine secretion (FDR = 1.8×10^{-3}) (Figure 4B; Table S3). Finally, in concordance with WT NK cells being enriched for pathways involved in blood coagulation (Figure 3B) and enhanced hemorrhaging in *CypD*$^{-/-}$ mice (Figures 1H and S1D), genes of hemostasis (FDR = 5.5×10^{-4}) and negative regulation of fibroblast growth factor production (FDR = 1.5×10^{-3}) were enriched in WT NK cells. Interestingly, one gene significantly upregulated in this pathway in WT cells, *Cd59a*, has previously been shown to mediate protection against IAV by inhibiting hemorrhaging and fibrosis in the lung (Longhi et al., 2007). Finally, genes showing significantly higher expression in WT mice were more likely to be found in the tissue repair gene set (Yanai et al., 2016) than expected by chance (p = 0.009), but not *CypD*$^{-/-}$ mice (p = 0.798) (Figure 4C).

CypD promotes NK cell lymphopoiesis and maturation in the bone marrow

To investigate whether a lack of mature NK cells in the BAL following infection in *CypD*$^{-/-}$ mice was due to alterations in proliferation or cell death, we analyzed Ki67 and active caspase 3 expression by flow cytometry and found no differences (Figures 5A and 5B). In addition to proliferation and cell death,

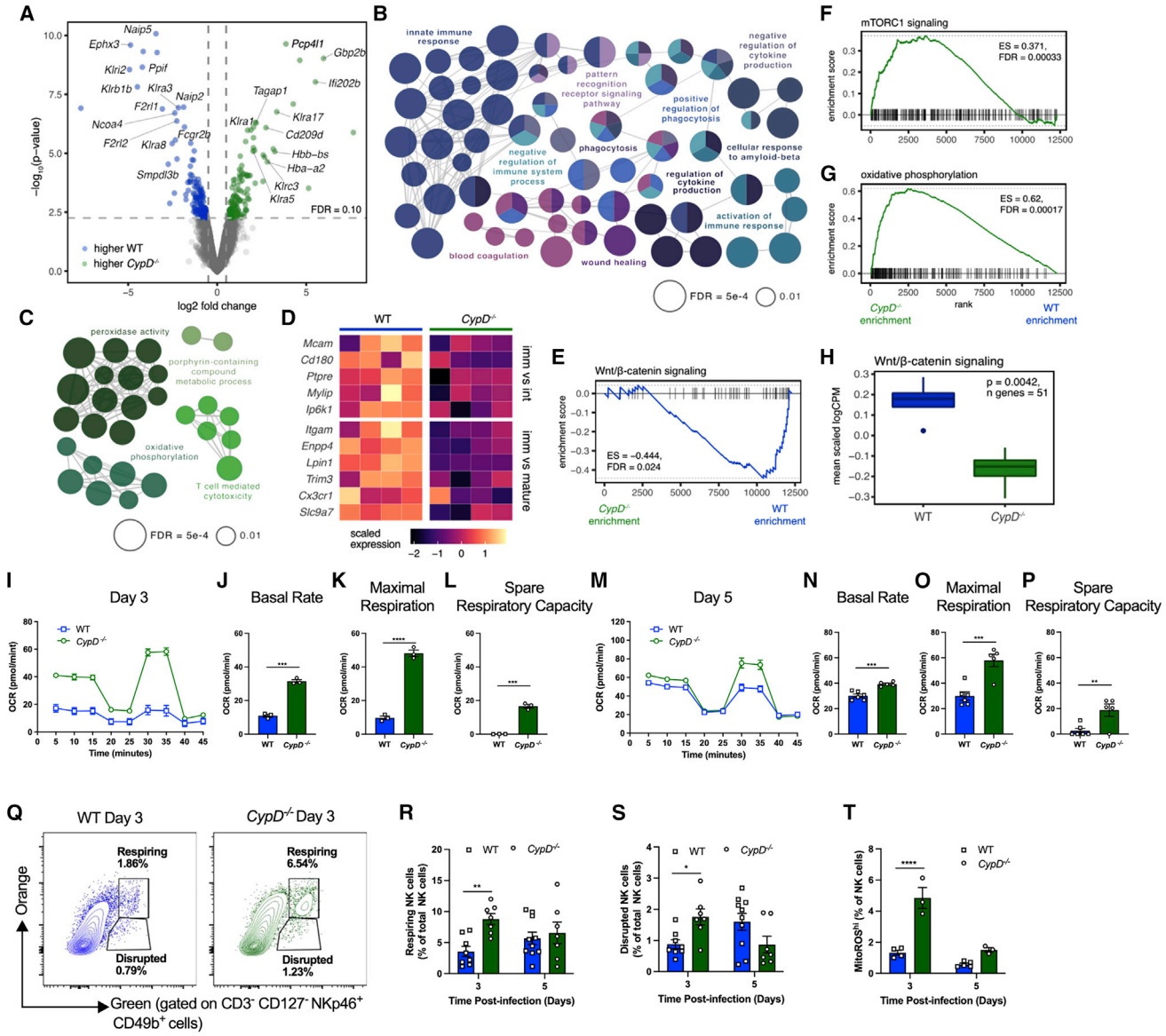

Figure 3. Transcriptomic profile and cellular metabolism of *CypD*$^{-/-}$ NK cells are altered after IAV infection

(A) Volcano plot of genes significantly differentially expressed (DE) between WT (blue, log2 fold change [FC] < −0.5; FDR < 0.10) and *CypD*$^{-/-}$ (green, log2 FC > 0.5; FDR < 0.10) NK cells. Genes with a negative log2 FC are higher in WT mice, while genes with a positive log2 FC are higher in *CypD*$^{-/-}$ mice.

(B and C) Significant (FDR < 0.01) ClueGO pathway enrichments for genes showing higher expression (FDR < 0.10) in WT (B) or *CypD*$^{-/-}$ (C) NK cells.

(D) Heatmap showing expression levels for maturity marker genes as identified in Chiossone et al. (2009).

(E–G) Barcode enrichment plots for hallmark (E) Wnt/β-catenin signaling, (F) mTORC1 signaling, and (G) oxidative phosphorylation pathways.

(H) Average, scaled logCPM expression estimates across genes in the hallmark Wnt/β-catenin signaling pathway.

(I–P) Oxygen consumption of NK cells. (I and M) Seahorse curves of (J–L) and (N–P), respectively.

(Q–S) Representative flow plots (Q) of NK cells stained with Mitotracker Orange and Green, as quantified in (R) and (S).

(T) Frequency of MitoSox Red^{hi} NK cells.

(I–P) All data are from one representative experiment of two, and each dot is a technical replicate from five pooled mice. (Q–T) Data are compiled from two experiments, and each dot represents a mouse. Statistics assessed by Student's t test (J–L and N–P) or two-way ANOVA followed by Sidak's multiple comparisons test (R–T). ES, enrichment score; *p<0.05, **p<0.01, ***p<0.001, ****p<0.0001. See also Figure S3.

aberrant recruitment into the airways could be responsible. CCR2 expression on NK cells is known to specifically facilitate migration of NK cells into the airways, but not the lung, which is instead mediated by CXCR3 (Carlin et al., 2018; van Helden et al., 2012). However, the frequency of CCR2^{+} NK cells was indistinguishable between WT and *CypD*$^{-/-}$ mice in the BAL, lung, and blood (Figures 5C, S4A, and S4B), confirming CCR2-mediated migration of NK cells into the airways is not dependent on CypD expression.

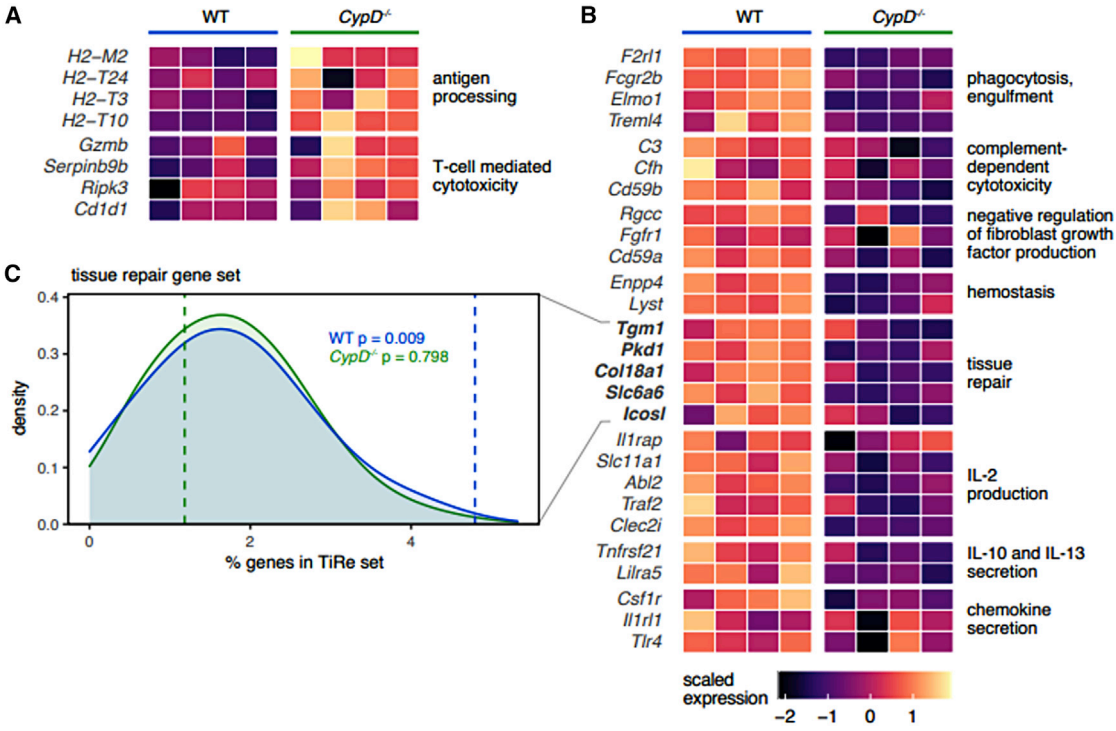

Figure 4. *CypD*$^{-/-}$ NK cells are differentially reprogrammed after IAV infection

(A and B) Heatmap showing expression levels (mean-centered and scaled) for selected subsets of genes that fall into ontology pathways and functional gene sets significantly enriched within WT or *CypD*$^{-/-}$ NK cells.

(C) Proportion of WT or *CypD*$^{-/-}$ differentially expressed genes that are in the tissue-repair dataset (Yanai et al., 2016) (WT, blue dashed line, p = 0.009; *CypD*$^{-/-}$, green dashed line, p = 0.798) compared with random expectation when sampling the same total number of WT or *CypD*$^{-/-}$ differentially expressed genes 1,000 times from all genes tested (null, density distributions).

Although on-demand egress of NK cells from the BM to peripheral tissues is well described, there is an additional population of tissue-resident NK cells that expresses CD49a rather than CD49b (Peng et al., 2013). This population is most prevalent in the uterus but can be found elsewhere, including the lung (Sojka et al., 2014). As expected, the vast majority of NK cells from the BAL and lungs were CD49b^{+} CD49a^{-}, indicative of a predominantly blood-derived population, and this frequency was the same in both groups (Figures 5D and S4C). However, the frequency of NK cells in the blood was decreased in *CypD*$^{-/-}$ mice (Figure 5E), and there were less fully mature CD27^{-} CD11b^{+} cells at day 5 post-IAV infection (Figures 5F, 5G, S4D, and S4E), suggesting the resident NK cell dynamics was not altered in *CypD*$^{-/-}$ mice.

The reduction of mature recruited NK cells led us to speculate that there was a defect in the generation of NK cells in *CypD*$^{-/-}$ mice. NK cell generation occurs through a progression of progenitors to fully mature effector NK cells (Figure 6A). Downstream of the pluripotent LKS population, cells of the lymphoid lineage and the myeloid and erythroid lineage separate through the common lymphoid progenitor (CLP) (Lin^{-} CD127^{+} cKit^{lo} Sca1^{lo}) and the common myeloid progenitor (CMP) (Lin^{-} CD127^{-} cKit^{+} Sca1^{-} CD34^{+} CD16/32^{-}), respectively. From the CLP, NK cells are generated first from the pre-NK progenitor (pre-NKP) (Lin^{-} CD127^{+} CD27^{+} CD122^{-} CD244.2^{+}), then the NKP (Lin^{-} CD127^{+} CD27^{+} CD122^{+} CD244.2^{+}), and finally *bona fide* NK cells that express NKp46 and CD49b (Abel et al., 2018). We phenotyped BM precursors during homeostasis and upon IAV infection to screen for hematopoietic changes in *CypD*$^{-/-}$ BM. We observed no differences in the frequency or number of LKS or CLP pouplations (Figures 6B, 6C, S4F, and S4G). In addition, there were similar levels of the CMP and granulocyte-macrophage progenitor (GMP) in WT and *CypD*$^{-/-}$ mice (Figures S4H and S4I). However, we observed a decrease in pre-NKP and NKP populations (Figures 6D–6F), as well as a lower frequency of fully mature CD11b^{+} CD27^{-} NK cells in the BM post-IAV infection (Figures 6G and S4J). Thus, CypD mediates NK cell hematopoiesis and an inability to progress through the NK cell lineage correlates with a reduction of mature NK cells in the periphery.

CypD$^{-/-}$ NK cell progenitors express higher levels of p53 and undergo enhanced cell death in the BM

To investigate the reduction of NK cell progenitors in the BM of *CypD*$^{-/-}$ mice, we evaluated both cell proliferation and death (Smith et al., 2018; Yamashita and Passegue, 2019). Both at steady state and uponIAV infection, CypD had no effect on proliferation (Figures S4K and S4L). Interestingly, p53, a central regulator of cell growth arrest and cell death (Brady and Attardi, 2010), has been demonstrated to interact with CypD to facilitate necrosis of structural cells (Vaseva et al., 2012) and CypD

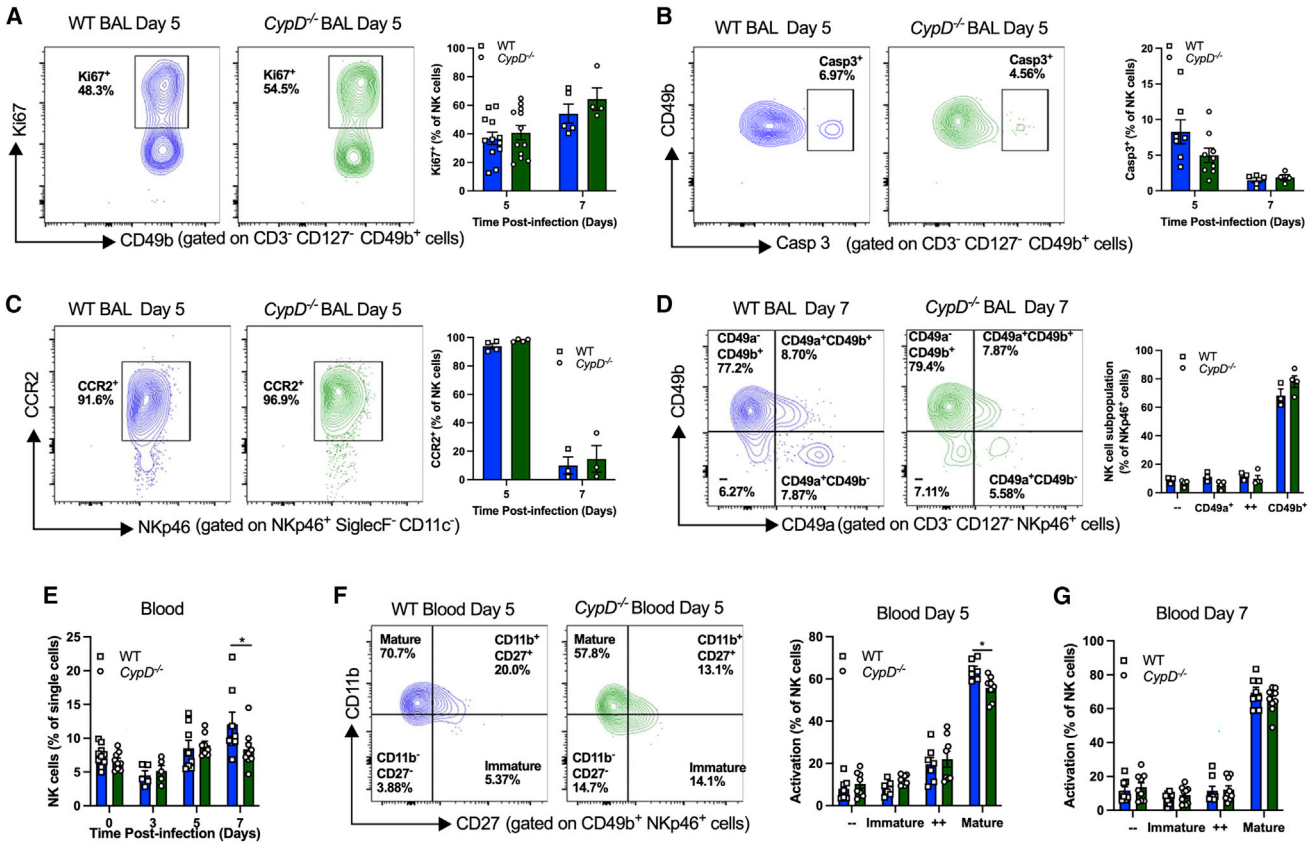

Figure 5. Frequency of NK cells is reduced in circulation of *CypD*$^{-/-}$ mice

(A–G) WT and *CypD*$^{-/-}$ mice were infected with IAV (50 PFU).

(A) Ki67 expression in NK cells in the BAL.

(B) NK cell expression of active caspase 3 in the BAL.

(C) CCR2 expression on NK cells of the BAL.

(D) Expression of CD49b versus CD49a on NK cells of the BAL.

(E–G) Peripheral blood was collected and the frequency of NK cells (E) and their activation state as defined by CD27 and CD11b expression (F and G) were quantified.

Left panels show a representative flow plot as quantified on the right. Each panel is a compilation of at least two experiments, except (C), which is one of two independent experiments. Each symbol represents one mouse. Statistics were assessed by two-way ANOVA followed by Sidak's multiple comparisons test; *p<0.05. See also Figure S4.

antagonizes p53-dependent growth arrest (Bigi et al., 2016). Moreover, p53 halts lymphopoiesis, causes cell death specifically in the lymphoid lineage, and leads to lymphopenia (Belle et al., 2015; Mendrysa et al., 2003). We thus investigated the level of p53 in NK cell progenitors and found elevated p53 protein in *CypD*$^{-/-}$ pre-NKPs (Figure 6H) and NKPs (Figure 6I), but not in effector NK cells in the BM (Figure S4M) or BAL (Figure S4N). Using differential expression of AnnexinV/NucSpot, we observed an enhanced frequency of dead (AnnexinV^{+} NucSpot^{+}) NKP cells (Figure 6J), but not pre-NKP cells (Figure S4O). Collectively, our results suggest that CypD antagonizes p53-mediated cell death in NK cell progenitors.

Susceptibility of *CypD*$^{-/-}$ mice to IAV is due to profound reduction of IL-22-producing NK cells

Having established that CypD regulates NK cell hematopoiesis and that *CypD*$^{-/-}$ NK cells are more phenotypically immature, we finally investigated whether NK cells from *CypD*$^{-/-}$ mice confer susceptibility to IAV infection. As the RNA-seq data indicated impaired anti-inflammatory cytokine production and wound healing pathways in *CypD*$^{-/-}$ NK cells (Figures 4B and 4C), we speculated that altered cytokine production was responsible for the heightened pulmonary tissue damage.

Upon IAV infection, NK cells are a well-known source of IFN-γ (Long et al., 2008; Stegemann-Koniszewski et al., 2018). However, the function of IFN-γ in response to IAV is controversial (Califano et al., 2018; Graham et al., 1993; Weiss et al., 2010). At day 7 post-IAV infection, we observed a significant decrease of IFN-γ in the BAL of *CypD*$^{-/-}$ mice (Figure 7A). By stimulating with phorbol 12-myristate 13-acetate (PMA) and ionomycin, we confirmed that NK cells from the BAL and spleen were a substantial source of IFN-γ, and at day 5, post-IAV infection and the frequency of *CypD*$^{-/-}$ IFN-γ^{+} NK cells were significantly reduced (Figures 7B and S5A). However, as previously shown

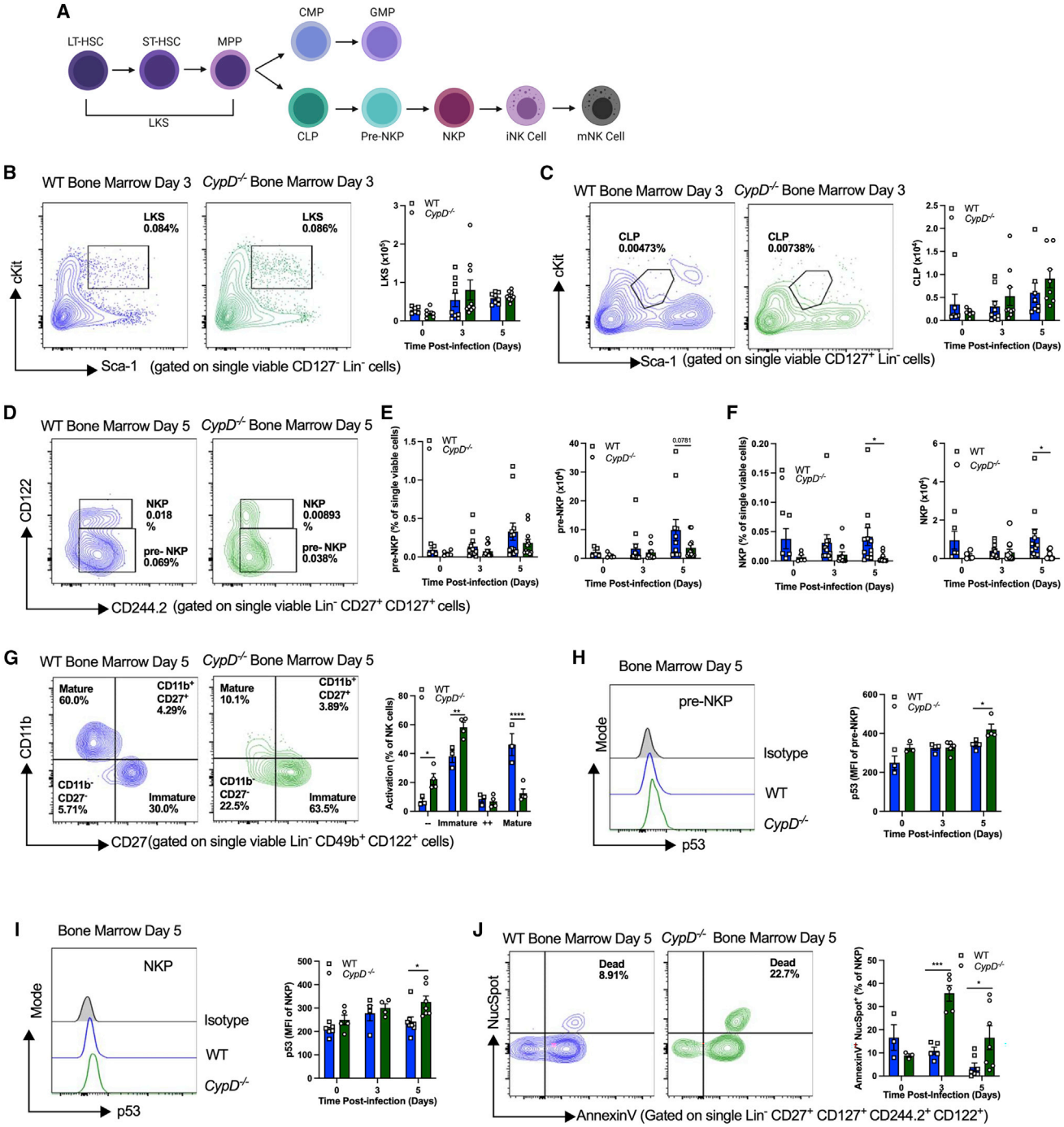

Figure 6. Bone marrow NK cell hematopoiesis is altered in IAV-infected *CypD*$^{-/-}$ mice

(A) Schematic of NK cell hematopoiesis starting at LKS cells to NK cells.

(B–G) Total cell counts of LKS (B), CLP (C), pre-natural killer progenitor (pre-NKP) (D and E), NKP (D and F), and activation statuses of NK cells (G). In (B), (C), (D), and (G), left panels are representative flow plots.

(H and I) Expression of p53 within pre-NKP (H) and NKP (I) populations. Left panels are representative histograms as quantified in the right panels.

(J) Expression of AnnexinV and NucSpot within the NKP.

(B)–(F), (I), and (J) are a compilation of at least two experiments, while (G) and (H) are one representative experiment of three independent experiments, with each symbol representing an individual mouse. Statistics are assessed by two-way ANOVA followed by Sidak's multiple comparisons test. *p<0.05, **p<0.01, ***p<0.001, ****p<0.0001. See also Figure S4.

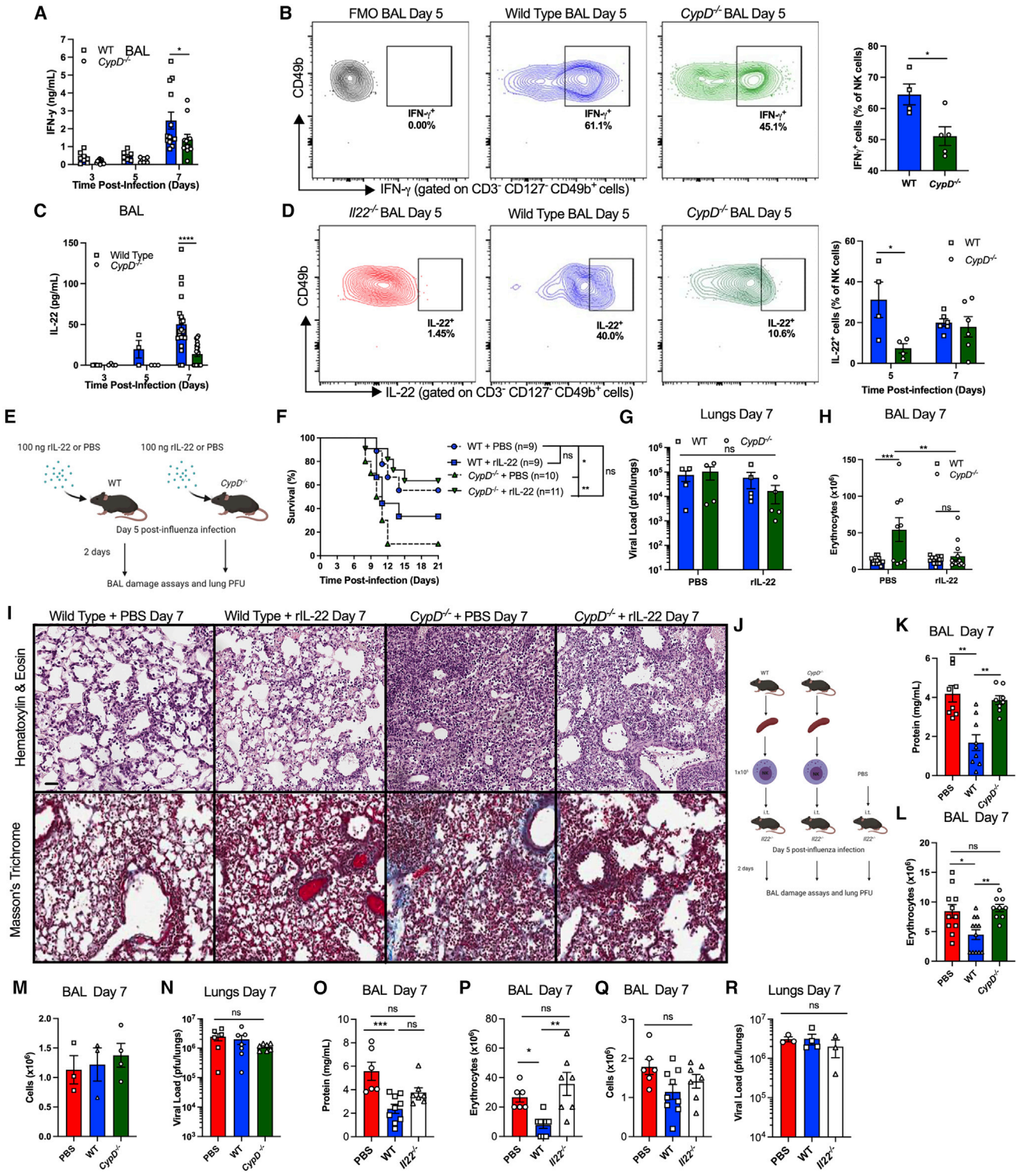

Figure 7. Reduced IL-22 production by NK cells is responsible for the susceptibility of *CypD*$^{-/-}$ mice to IAV

(A) Levels of IFN-γ in the BAL of infected WT and *CypD*$^{-/-}$ mice.

(B) Staining of IFN-γ in NK cells. Flow plots are representative and gated against the fluorescence minus one (FMO).

(C) Levels of IL-22 in the BAL of infected WT and *CypD*$^{-/-}$ mice.

(D) Staining for IL-22 in NK cells. Flow plots are representative and gated against an *Il22*$^{-/-}$ mouse.

(legend continued on next page)

(Graham et al., 1993), *Ifngr*$^{-/-}$ exhibited a similar amount of lung damage (Figures S5B and S5C), although an increase in leukocytes was noted (Figure S5D). To rule out that the reduction in IFN-γ was responsible for the damage in the *CypD*$^{-/-}$ mice, we reconstituted the airways of WT and *CypD*$^{-/-}$ mice with 100 ng of IFN-γ or vehicle intranasally at 5 days post-IAV infection and collected the BAL at 7 days. As expected, we observed a significant increase in protein and erythrocytes in the BAL of *CypD*$^{-/-}$ mice that received PBS compared with WT mice, but there was no amelioration in either group that received IFN-γ (Figures S5E and S5F). Collectively, these data confirm that, despite a reduction of NK-cell-derived IFN-γ in *CypD*$^{-/-}$ airways post-IAV infection, IFN-γ was not responsible for the break in disease tolerance.

NK cells are also an important source of IL-22 at barrier sites (Wolk et al., 2002; Zenewicz et al., 2008), including during IAV infection (Kumar et al., 2013; Pociask et al., 2013). Importantly, CD27^{-} NK cells, specifically, have been shown to be the major source of IL-22 upon infection (Guo and Topham, 2010). Thus, we postulated that a lack of IL-22 production by *CypD*$^{-/-}$ NK cells was underlying their susceptibility. To assess this, we began by confirming a previous study (Pociask et al., 2013), showing that IL-22-deficient mice had enhanced lung damage post-IAV infection (Figures S5G–S5I). Next, we measured the level of IL-22 in the BAL of WT and *CypD*$^{-/-}$ mice as well as littermate mice and found a significant reduction of IL-22 in *CypD*$^{-/-}$ mice (Figures 7C and S5J). Moreover, there was a reduction of IL-22^{+} NK cells in both the BAL and spleen of *CypD*$^{-/-}$ mice when compared to WT mice (Figures 7D and S5K), and purified *CypD*$^{-/-}$ NK cells from the spleens of infected mice exhibited lower *Il22* transcripts (Figure S5L). Interestingly, this phenomenon was cell extrinsic and dependent upon IAV infection, as purified NK cells from naive *CypD*$^{-/-}$ or WT mice produced similar levels of IL-22 upon *ex vivo* stimulation with IL-18 and IL-23 (Zenewicz et al., 2008; Figure S5M). A similar phenomenon was observed in WT and *CypD*$^{-/-}$ polarized CD4^{+} Th17 cells (Figure S5N). Thus, these data collectively confirm the importance of CypD within NK cells in IL-22 production during IAV infection.

Because *CypD*$^{-/-}$ mice have reduced IL-22 in the airways, we assessed whether or not reconstitution of *CypD*$^{-/-}$ mice with IL-22 could protect against IAV. At day 5 post-IAV infection with the lethal dose (90 PFU), we intranasally reconstituted the airways of WT and *CypD*$^{-/-}$ mice with 100 ng of IL-22 or PBS (Figure 7E) and assessed mortality. As expected, *CypD*$^{-/-}$ mice that received PBS were significantly more susceptible than WT mice that received PBS. Strikingly, the survival of *CypD*$^{-/-}$ mice that received IL-22 was significantly increased and comparable to both WT groups (Figure 7F). This enhanced survival was independent of host resistance (Figure 7G) but dependent on disease tolerance (Figures 7H, 7I, and S5O). We then sought to directly assess the capacity of WT versus *CypD*$^{-/-}$ NK cells to protect against tissue damage in an IL-22-deficient environment. To do this, we purified NK cells from naive spleens of WT and *CypD*$^{-/-}$ hosts and then transferred 1 × 10^{5} cells intratracheally into infected *Il22*$^{-/-}$ hosts at 5 days post-IAV infection. At day 7 post-IAV infection (2 days post-transfer), we collected the BAL and lungs to assess damage and viral loads (Figure 7J). We found that IL-22-deficient mice that received WT NK cells exhibited statistically significantly less tissue damage, while no improvement was noted in mice receiving *CypD*$^{-/-}$ NK cells (Figures 7K and 7L). In line with IL-22 acting primarily on structural cells, no variance in total leukocyte counts or pulmonary viral loads was observed in any groups (Figures 7M and 7N). The production of IL-22 by NK cells was required, as the transfer of *Il22*$^{-/-}$ NK cells equally had no protective effect (Figures S5P–S5S). Finally, we transferred NK cells from WT and *Il22*$^{-/-}$ hosts into *CypD*$^{-/-}$ mice. While WT NK cells were able to significantly lower lung hemorrhage (erythrocytes) and damage (protein levels), *Il22*$^{-/-}$ NK cells had no effect, and there were no differences in total cells or viral loads (Figures 7O–7R). Collectively, these data indicate that NK cell-derived IL-22 is dependent upon CypD and is required for regulating pulmonary disease tolerance following IAV infection.

DISCUSSION

The immune response to influenza virus requires a tightly regulated effort from both the innate and adaptive branches. Shortly following infection, early innate cells coordinate to resist and eliminate IAV from the lung (host resistance). However, host resistance comes at a substantial immunopathological cost that often is the cause of mortality; therefore, limiting tissue damage and maintaining the physiological function of the lung (disease tolerance) is critical for host survival.

Disease tolerance as a defense strategy was initially established in plants (Kover and Schaal, 2002) and has since been extended to mammals (Medzhitov et al., 2012; Schneider and Ayres, 2008). Evidence for its importance during chronic infection, such as *Mtb* and helminthic infections (Divangahi, 2018; King and Li, 2018), is accumulating. Yet our knowledge of disease tolerance pathways against acute infection remains limited, although preservation of barrier integrity seems integral. In the current study, we define a role for CypD in maintenance of the pulmonary epithelial and endothelial barrier. This work dovetails our earlier studies that highlighted CypD as an essential component of lymphocyte-mediated host defense (Condotta et al., 2020; Tzelepis et al., 2018).

(E) Model of experiments in (F–I).
(F–I) Survival following 90 PFU infection (F) or viral loads (G), erythrocytes in the BAL (H), and pulmonary H&E or Masson's trichrome staining (I; scale bar represents 30 μM) following 50 PFU infection.
(J) Model of experiments in (K–N).
(K–N) Assessment of protein (K), erythrocyte (L), and leukocyte levels in the BAL (M) or lung viral loads (N) of *Il22*$^{-/-}$ recipients.
(O–R) Assessment of protein (O), erythrocyte (P), and leukocyte levels in the BAL (Q) or lung viral loads (R) in *CypD*$^{-/-}$ recipients.
In (A), (C), (F), (H), (K), (L), (N), and (O–R), data are combinations of at least two experiments. (B), (D), (G), and (M) are from one experiment of at least two experiments. (I) is representative of three or four mice. In (A–D), (G), (H), and (K–R), each symbol represents a mouse, and in (F), n values are displayed. Statistical tests are as follows: (A–D, G, and H) two-way ANOVA followed by Sidak's multiple comparisons test, (F) log rank test, and (K–R) one-way ANOVA followed by Dunnett's test or Kruskal-Wallis test. *p<0.05, **p<0.01, ***p<0.001, ****p<0.0001. See also Figure S5.

All members of the cyclophilin family are highly conserved in humans (Giorgio et al., 2010), and they have been extensively implicated in host resistance to viral infection (Frausto et al., 2013). CypD is the only member of the family that translocates to the mitochondrial matrix, which places it at the intersection of several essential cellular processes during host defense. For example, in mature leukocytes, the mitochondrial antiviral signaling (MAVS) protein is anchored to the outer mitochondrial membrane and is essential for the induction of IFN-I in response to several viruses, including IAV (Jaworska et al., 2014; West et al., 2011) and lymphocytic choriomeningitis virus (LCMV) (Wu et al., 2016). On the other hand, we highlighted the importance of CypD-dependent metabolic changes in T cell responses to promote disease tolerance to *Mtb* (Tzelepis et al., 2018). Thus, mitochondria are critical orchestrators of both resistance and tolerance mechanisms in ways that are cell and pathogen specific.

This study also revealed a role for CypD in promoting lymphopoiesis, potentially by inhibiting p53-associated progenitor cell death. In structural cells, p53 can translocate to the mitochondrial matrix and interact with CypD, resulting in necrotic cell death (Vaseva et al., 2012). In hematopoiesis, p53 activity specifically within lymphocyte progenitors has been shown to induce cell death to skew hematopoiesis toward myelopoiesis and cell death is an emerging master regulator of lineage bias (Kanayama et al., 2017; Khan et al., 2020; Smith et al., 2018). We speculate that inhibition of p53 by CypD in NK cell progenitors promotes lymphopoiesis, akin to the role previously described for Mysm1 and Mdm2 (Belle et al., 2015; Mendrysa et al., 2003).

Conventional NK cells are well known for their tumoricidal capacity and cytotoxicity against virally infected cells (Vivier et al., 2008). Yet NK cells appear to participate in both host resistance and disease tolerance during IAV infection. For example, complete genetic ablation of NK cells (Li et al., 2017), loss of the HA-interacting receptor NKp46 (Gazit et al., 2006), or depletion (Stein-Streilein and Guffee, 1986) all result in IAV-induced lethality due to elevated viral titers in the lung and loss of host resistance, while IL-22 production by NK cells limits pulmonary immunopathology (Kumar et al., 2013). Here, we found that CypD regulates this IL-22 production by NK cells (Figures 7C, 7D, and S5K), while expression of perforin and granzyme B by NK cells (Figure 2H) and viral loads (Figure 1C) were unaffected. Therefore, during the course of IAV infection, the functional capacity of NK cells is dynamic and can be changed from promoting resistance to tolerance.

Early NK cell responses appear to be mediated by NKp46 and are primarily concerned with restricting viral replication by killing infected cells. Following viral containment, NK cells may shift to promote disease tolerance through the production of IL-22 at around day 5 p.i. Our results suggest that, during the early phase of infection, NK cell function is CypD independent, while at the later stage of infection, it is mediated by CypD. Furthermore, IL-22 can be produced by several lymphocyte populations in response to IAV. Studies investigating the early phase of infection elucidated NKT and other ILCs as the major sources (Ivanov et al., 2013; Paget et al., 2012), while another's work at a later phase of infection (Kumar et al., 2013) showed conventional NK cells as the major source of IL-22. Our adoptive transfer experiments of NK cells at day 5 p.i. into *Il22*$^{-/-}$ and *CypD*$^{-/-}$ mice support the importance of NK cells at this later time point in the production of IL-22 and disease tolerance (Figure 7).

Influenza infections are persistent human pathogens, being responsible yearly for approximately 1 billion infections and 500,000 deaths worldwide (Krammer et al., 2018). Past IAV pandemics have highlighted the importance of understanding host-pathogen interactions during acute respiratory infections. As we continue to better appreciate the relationship between early host resistance and later disease tolerance responses, potential therapies require appropriate timing. For instance, our studies investigating host immunotherapy via the eicosanoid/IFN-I axis showed early inhibition of mPGES-1 increased antiviral IFN-β production to enhance host resistance (Coulombe et al., 2014). On the other hand, late-stage administration of exogenous LTB_4 potentiates immunomodulation of IFN-α signaling to promote disease tolerance (Pernet et al., 2019). Considering that higher levels of lung immunopathology is the major cause of morbidity and mortality during many respiratory infections, including severe acute respiratory syndrome coronavirus 2 (SARS-CoV-2) (Ayres, 2020; Tay et al., 2020), next-generation therapies that target disease tolerance may provide a more universal benefit compared with specific antiviral therapies.

Limitations of the study

Our study provides insight into the role of CypD in NK biology during IAV infection and the complex interplay of host-pathogen interactions. However, we also identify several limitations in our work that require further investigation, including:

(1) Genetics: Our RNA-seq and Seahorse data highlight elevated reliance on OXPHOS in *CypD*$^{-/-}$ NK cells compared to WT NK cells, suggesting a metabolic shift in NK cells may promote IL-22 production. However, more study into the transcriptional landscape of this metabolic shift, CypD, and cytokine production is needed.
(2) Protein-protein interactions: The increased levels of p53 and cell death in *CypD*$^{-/-}$ NKP suggest that CypD may interact with p53 to block cell death and promote lymphopoiesis. Direct study using protein-protein interaction techniques is required to investigate this hypothesis.
(3) Immune response: We outline a role for CypD NK cell development in the BM and NK cell function in the airways. Our work does not provide a direct link between these functions of CypD; however, they may be interconnected. Usage of conditional, rather than constitutive, knockouts in lymphoid progenitors and mature NK cells will address this question.

STAR★METHODS

Detailed methods are provided in the online version of this paper and include the following:

- KEY RESOURCES TABLE
- RESOURCE AVAILABILITY
  - Lead contact

SUPPLEMENTAL INFORMATION

Supplemental information can be found online at https://doi.org/10.1016/j.celrep.2022.110974.

ACKNOWLEDGMENTS

The authors would like to thank members of the Small Animal Imaging Labs, particularly Dr. Barry Bedell and Mathieu Simard, and the Histopathology Core of the RI-MUHC, as well members of the Institut de Recherches Cliniques de Montréal for the generation and sequencing of RNA-seq libraries. Models were created by BioRender.com. This work was supported by the Canadian Institute of Health Research Project Grant (168885) to M.D. M.D. holds a Fonds de Recherche du Québec–Santé Award and the Strauss Chair in Respiratory Diseases. J.D. was supported by the Molson Foundation Award and H.E.R. by a National Science Foundation Graduate Research Fellowship (DGE-1746045).

AUTHOR CONTRIBUTIONS

M.D. conceived and supervised the project. J.D. and M.D. designed the experiments; J.D., E.P., and K.A.T. performed experiments. Data were analyzed and interpreted by J.D. and M.D., except for RNA-seq data analyses, which were performed by H.E.R., under the supervision of L.B.B. I.L.K. and S.A.K provided technical input, expertise, and manuscript review. J.D., H.E.R., L.B.B., and M.D. wrote the manuscript.

DECLARATION OF INTERESTS

The authors declare no competing interests.

Received: July 27, 2021
Revised: March 25, 2022
Accepted: May 26, 2022
Published: June 21, 2022

REFERENCES

Abel, A.M., Yang, C., Thakar, M.S., and Malarkannan, S. (2018). Natural killer cells: development, maturation, and clinical utilization. Front. Immunol. *9*, 1869. https://doi.org/10.3389/fimmu.2018.01869.

Aldridge, J.R., Jr., Moseley, C.E., Boltz, D.A., Negovetich, N.J., Reynolds, C., Franks, J., Brown, S.A., Doherty, P.C., Webster, R.G., and Thomas, P.G. (2009). TNF/iNOS-producing dendritic cells are the necessary evil of lethal influenza virus infection. Proc. Natl. Acad. Sci. U S A *106*, 5306–5311. https://doi.org/10.1073/pnas.0900655106.

Ayres, J.S. (2020). Surviving COVID-19: a disease tolerance perspective. Sci. Adv. *6*, eabc1518. https://doi.org/10.1126/sciadv.abc1518.

Baines, C.P., Kaiser, R.A., Purcell, N.H., Blair, N.S., Osinska, H., Hambleton, M.A., Brunskill, E.W., Sayen, M.R., Gottlieb, R.A., Dorn, G.W., et al. (2005). Loss of cyclophilin D reveals a critical role for mitochondrial permeability transition in cell death. Nature *434*, 658–662. https://doi.org/10.1038/nature03434.

Bautista, E., Chotpitayasunondh, T., Gao, Z., Harper, S.A., Shaw, M., Uyeki, T.M., Zaki, S.R., Hayden, F.G., Hui, D.S., Kettner, J.D., et al. (2010). Clinical aspects of pandemic 2009 influenza A (H1N1) virus infection. N. Engl. J. Med. *362*, 1708–1719. https://doi.org/10.1056/NEJMra1000449.

Belle, J.I., Langlais, D., Petrov, J.C., Pardo, M., Jones, R.G., Gros, P., and Nijnik, A. (2015). p53 mediates loss of hematopoietic stem cell function and lymphopenia in Mysm1 deficiency. Blood *125*, 2344–2348. https://doi.org/10.1182/blood-2014-05-574111.

Bigi, A., Beltrami, E., Trinei, M., Stendardo, M., Pelicci, P.G., Giorgio, M., and Bigi, A. (2016). Cyclophilin D counteracts P53-mediated growth arrest and promotes Ras tumorigenesis. Oncogene *35*, 5132–5143. https://doi.org/10.1038/onc.2016.42.

Bindea, G., Mlecnik, B., Hackl, H., Charoentong, P., Tosolini, M., Kirilovsky, A., Fridman, W.H., Pagès, F., Trajanoski, Z., and Galon, J. (2009). ClueGO: a Cytoscape plug-in to decipher functionally grouped gene ontology and pathway annotation networks. Bioinformatics *25*, 1091–1093. https://doi.org/10.1093/bioinformatics/btp101.

Brady, C.A., and Attardi, L.D. (2010). p53 at a glance. J. Cell Sci. *123*, 2527–2532. https://doi.org/10.1242/jcs.064501.

Brandes, M., Klauschen, F., Kuchen, S., and Germain, R.N. (2013). A systems analysis identifies a feedforward inflammatory circuit leading to lethal influenza infection. Cell *154*, 197–212. https://doi.org/10.1016/j.cell.2013.06.013.

Bray, N.L., Pimentel, H., Melsted, P., and Pachter, L. (2016). Near-optimal probabilistic RNA-seq quantification. Nat. Biotechnol. *34*, 525–527. https://doi.org/10.1038/nbt.3519.

Califano, D., Furuya, Y., Roberts, S., Avram, D., McKenzie, A.N.J., and Metzger, D.W. (2018). IFN-gamma increases susceptibility to influenza A infection through suppression of group II innate lymphoid cells. Mucosal Immunol. *11*, 209–219. https://doi.org/10.1038/mi.2017.41.

Carlin, L.E., Hemann, E.A., Zacharias, Z.R., Heusel, J.W., and Legge, K.L. (2018). Natural killer cell recruitment to the lung during influenza A virus infection is dependent on CXCR3, CCR5, and virus exposure dose. Front. Immunol. *9*, 781. https://doi.org/10.3389/fimmu.2018.00781.

Chiossone, L., Chaix, J., Fuseri, N., Roth, C., Vivier, E., and Walzer, T. (2009). Maturation of mouse NK cells is a 4-stage developmental program. Blood *113*, 5488–5496. https://doi.org/10.1182/blood-2008-10-187179.

Collin, R., St-Pierre, C., Guilbault, L., Mullins-Dansereau, V., Policheni, A., Guimont-Desrochers, F., Pelletier, A.N., Gray, D.H., Drobetsky, E., Perreault, C., et al. (2017). An unbiased linkage approach reveals that the p53 pathway is coupled to NK cell maturation. J. Immunol. *199*, 1490–1504. https://doi.org/10.4049/jimmunol.1600789.

Condotta, S.A., Downey, J., Pardy, R.D., Valbon, S.F., Tarrab, E., Lamarre, A., Divangahi, M., and Richer, M.J. (2020). Cyclophilin D regulates antiviral CD8(+) T cell survival in a cell-extrinsic manner. Immunohorizons *4*, 217–230. https://doi.org/10.4049/immunohorizons.2000016.

Coulombe, F., Jaworska, J., Verway, M., Tzelepis, F., Massoud, A., Gillard, J., Wong, G., Kobinger, G., Xing, Z., Couture, C., et al. (2014). Targeted prostaglandin E2 inhibition enhances antiviral immunity through induction of type I interferon and apoptosis in macrophages. Immunity *40*, 554–568. https://doi.org/10.1016/j.immuni.2014.02.013.

Crinier, A., Milpied, P., Escalière, B., Piperoglou, C., Galluso, J., Balsamo, A., Spinelli, L., Cervera-Marzal, I., Ebbo, M., Girard-Madoux, M., et al. (2018). High-dimensional single-cell analysis identifies organ-specific signatures and conserved NK cell subsets in humans and mice. Immunity *49*, 971–986.e5. https://doi.org/10.1016/j.immuni.2018.09.009.

Dawson, T.C., Beck, M.A., Kuziel, W.A., Henderson, F., and Maeda, N. (2000). Contrasting effects of CCR5 and CCR2 deficiency in the pulmonary

inflammatory response to influenza A virus. Am. J. Pathol. *156*, 1951–1959. https://doi.org/10.1016/S0002-9440(10)65068-7.

Divangahi, M. (2018). Are tolerance and training required to end TB? Nat. Rev. Immunol. *18*, 661–663. https://doi.org/10.1038/s41577-018-0070-y.

Downey, J., Pernet, E., Coulombe, F., and Divangahi, M. (2018). Dissecting host cell death programs in the pathogenesis of influenza. Microbes Infect. *20*, 560–569. https://doi.org/10.1016/j.micinf.2018.03.005.

Frausto, S.D., Lee, E., and Tang, H.L. (2013). Cyclophilins as modulators of viral replication. Viruses *5*, 1684–1701. https://doi.org/10.3390/v5071684.

Fu, B., Wang, F., Sun, R., Ling, B., Tian, Z., and Wei, H. (2011). CD11b and CD27 reflect distinct population and functional specialization in human natural killer cells. Immunology *133*, 350–359. https://doi.org/10.1111/j.1365-2567.2011.03446.x.

Gazit, R., Gruda, R., Elboim, M., Arnon, T.I., Katz, G., Achdout, H., Hanna, J., Qimron, U., Landau, G., Greenbaum, E., et al. (2006). Lethal influenza infection in the absence of the natural killer cell receptor gene Ncr1. Nat. Immunol. *7*, 517–523. https://doi.org/10.1038/ni1322.

Ghoneim, H.E., Thomas, P.G., and McCullers, J.A. (2013). Depletion of alveolar macrophages during influenza infection facilitates bacterial superinfections. J. Immunol. *191*, 1250–1259. https://doi.org/10.4049/jimmunol.1300014.

Giorgio, V., Soriano, M.E., Basso, E., Bisetto, E., Lippe, G., Forte, M.A., and Bernardi, P. (2010). Cyclophilin D in mitochondrial pathophysiology. Biochim. Biophys. Acta *1797*, 1113–1118. https://doi.org/10.1016/j.bbabio.2009.12.006.

Glasner, A., Zurunic, A., Meningher, T., Lenac Rovis, T., Tsukerman, P., Bar-On, Y., Yamin, R., Meyers, A.F.A., Mandeboim, M., Jonjic, S., and Mandelboim, O. (2012). Elucidating the mechanisms of influenza virus recognition by Ncr1. PLoS One *7*, e36837. https://doi.org/10.1371/journal.pone.0036837.

Graham, M.B., Dalton, D.K., Giltinan, D., Braciale, V.L., Stewart, T.A., and Braciale, T.J. (1993). Response to influenza infection in mice with a targeted disruption in the interferon gamma gene. J. Exp. Med. *178*, 1725–1732. https://doi.org/10.1084/jem.178.5.1725.

Guo, H.L., and Topham, D.J. (2010). Interleukin-22 (IL-22) production by pulmonary natural killer cells and the potential role of IL-22 during primary influenza virus infection. J. Virol. *84*, 7750–7759. https://doi.org/10.1128/Jvi.00187-10.

Herold, S., Steinmueller, M., von Wulffen, W., Cakarova, L., Pinto, R., Pleschka, S., Mack, M., Kuziel, W.A., Corazza, N., Brunner, T., et al. (2008). Lung epithelial apoptosis in influenza virus pneumonia: the role of macrophage-expressed TNF-related apoptosis-inducing ligand. J. Exp. Med. *205*, 3065–3077. https://doi.org/10.1084/jem.20080201.

Ip, W.K.E., Hoshi, N., Shouval, D.S., Snapper, S., and Medzhitov, R. (2017). Anti-inflammatory effect of IL-10 mediated by metabolic reprogramming of macrophages. Science *356*, 513–519. https://doi.org/10.1126/science.aal3535.

Ivanov, S., Renneson, J., Fontaine, J., Barthelemy, A., Paget, C., Fernandez, E.M., Blanc, F., De Trez, C., Van Maele, L., Dumoutier, L., et al. (2013). Interleukin-22 reduces lung inflammation during influenza A virus infection and protects against secondary bacterial infection. J. Virol. *87*, 6911–6924. https://doi.org/10.1128/Jvi.02943-12.

Jaworska, J., Coulombe, F., Downey, J., Tzelepis, F., Shalaby, K., Tattoli, I., Berube, J., Rousseau, S., Martin, J.G., Girardin, S.E., et al. (2014). NLRX1 prevents mitochondrial induced apoptosis and enhances macrophage antiviral immunity by interacting with influenza virus PB1-F2 protein. Proc. Natl. Acad. Sci. U S A *111*, E2110–E2119. https://doi.org/10.1073/pnas.1322118111.

Kanayama, M., Xu, S., Danzaki, K., Gibson, J.R., Inoue, M., Gregory, S.G., and Shinohara, M.L. (2017). Skewing of the population balance of lymphoid and myeloid cells by secreted and intracellular osteopontin. Nat. Immunol. *18*, 973–984. https://doi.org/10.1038/ni.3791.

Khan, N., Downey, J., Sanz, J., Kaufmann, E., Blankenhaus, B., Pacis, A., Pernet, E., Ahmed, E., Cardoso, S., Nijnik, A., et al. (2020). M. tuberculosis reprograms hematopoietic stem cells to limit myelopoiesis and impair trained immunity. Cell *183*, 752–770.e22. https://doi.org/10.1016/j.cell.2020.09.062.

King, I.L., and Li, Y. (2018). Host–parasite interactions promote disease tolerance to intestinal helminth infection. Front. Immunol. *9*, 2128. https://doi.org/10.3389/fimmu.2018.02128.

Korotkevich, G., Sukhov, V., and Sergushichev, A. (2019). Fast gene set enrichment analysis. Preprint at bioRxiv. https://doi.org/10.1101/060012.

Kover, P.X., and Schaal, B.A. (2002). Genetic variation for disease resistance and tolerance among Arabidopsis thaliana accessions. Proc. Natl. Acad. Sci. U S A *99*, 11270–11274. https://doi.org/10.1073/pnas.102288999.

Krammer, F., Smith, G.J.D., Fouchier, R.A.M., Peiris, M., Kedzierska, K., Doherty, P.C., Palese, P., Shaw, M.L., Treanor, J., Webster, R.G., and García-Sastre, A. (2018). Influenza. Nat. Rev. Dis. Primers *4*, 3. https://doi.org/10.1038/s41572-018-0002-y.

Kumar, P., Thakar, M.S., Ouyang, W., and Malarkannan, S. (2013). IL-22 from conventional NK cells is epithelial regenerative and inflammation protective during influenza infection. Mucosal Immunol. *6*, 69–82. https://doi.org/10.1038/mi.2012.49.

Leung, N.H.L., Xu, C., Ip, D.K.M., and Cowling, B.J. (2015). Review article: the fraction of influenza virus infections that are asymptomatic: a systematic review and meta-analysis. Epidemiology *26*, 862–872. https://doi.org/10.1097/EDE.0000000000000340.

Li, T., Wang, J., Wang, Y., Chen, Y., Wei, H., Sun, R., and Tian, Z. (2017). Respiratory influenza virus infection induces memory-like liver NK cells in mice. J. Immunol. *198*, 1242–1252. https://doi.org/10.4049/jimmunol.1502186.

Liberzon, A., Birger, C., Thorvaldsdóttir, H., Ghandi, M., Mesirov, J.P., and Tamayo, P. (2015). The molecular signatures database hallmark gene set collection. Cell Syst. *1*, 417–425. https://doi.org/10.1016/j.cels.2015.12.004.

Lin, K.L., Suzuki, Y., Nakano, H., Ramsburg, E., and Gunn, M.D. (2008). CCR2+ monocyte-derived dendritic cells and exudate macrophages produce influenza-induced pulmonary immune pathology and mortality. J. Immunol. *180*, 2562–2572. https://doi.org/10.4049/jimmunol.180.4.2562.

Long, B.R., Michaelsson, J., Loo, C.P., Ballan, W.M., Vu, B.-A.N., Hecht, F.M., Lanier, L.L., Chapman, J.M., and Nixon, D.F. (2008). Elevated frequency of gamma interferon-producing NK cells in healthy adults vaccinated against influenza virus. Clin. Vaccine Immunol. *15*, 120–130. https://doi.org/10.1128/cvi.00357-07.

Longhi, M.P., Williams, A., Wise, M., Morgan, B.P., and Gallimore, A. (2007). CD59a deficiency exacerbates influenza-induced lung inflammation through complement-dependent and -independent mechanisms. Eur. J. Immunol. *37*, 1266–1274. https://doi.org/10.1002/eji.200636755.

Mandelboim, O., Lieberman, N., Lev, M., Paul, L., Arnon, T.I., Bushkin, Y., Davis, D.M., Strominger, J.L., Yewdell, J.W., and Porgador, A. (2001). Recognition of haemagglutinins on virus-infected cells by NKp46 activates lysis by human NK cells. Nature *409*, 1055–1060. https://doi.org/10.1038/35059110.

Marçais, A., Cherfils-Vicini, J., Viant, C., Degouve, S., Viel, S., Fenis, A., Rabilloud, J., Mayol, K., Tavares, A., Bienvenu, J., et al. (2014). The metabolic checkpoint kinase mTOR is essential for IL-15 signaling during the development and activation of NK cells. Nat. Immunol. *15*, 749–757. https://doi.org/10.1038/ni.2936.

Martin, M. (2011). Cutadapt removes adapter sequences from high-throughput sequencing reads. EMBnet.J. *17*, 3. https://doi.org/10.14806/ej.17.1.200.

Martins, R., Carlos, A.R., Braza, F., Thompson, J.A., Bastos-Amador, P., Ramos, S., and Soares, M.P. (2019). Disease tolerance as an inherent component of immunity. Annu. Rev. Immunol. *37*, 405–437. https://doi.org/10.1146/annurev-immunol-042718-041739.

McAleer, J.P., and Kolls, J.K. (2014). Directing traffic: IL-17 and IL-22 coordinate pulmonary immune defense. Immunol. Rev. *260*, 129–144. https://doi.org/10.1111/imr.12183.

Medzhitov, R., Schneider, D.S., and Soares, M.P. (2012). Disease tolerance as a defense strategy. Science *335*, 936–941. https://doi.org/10.1126/science.1214935.

Mendrysa, S.M., McElwee, M.K., Michalowski, J., O'Leary, K.A., Young, K.M., and Perry, M.E. (2003). mdm2 Is critical for inhibition of p53 during

lymphopoiesis and the response to ionizing irradiation. Mol. Cell. Biol. *23*, 462–472. https://doi.org/10.1128/mcb.23.2.462-473.2003.

Meunier, I., Kaufmann, E., Downey, J., and Divangahi, M. (2017). Unravelling the networks dictating host resistance versus tolerance during pulmonary infections. Cell Tissue Res. *367*, 525–536. https://doi.org/10.1007/s00441-017-2572-5.

Nakagawa, T., Shimizu, S., Watanabe, T., Yamaguchi, O., Otsu, K., Yamagata, H., Inohara, H., Kubo, T., and Tsujimoto, Y. (2005). Cyclophilin D-dependent mitochondrial permeability transition regulates some necrotic but not apoptotic cell death. Nature *434*, 652–658. https://doi.org/10.1038/nature03317.

Narasaraju, T., Yang, E., Samy, R.P., Ng, H.H., Poh, W.P., Liew, A.A., Phoon, M.C., van Rooijen, N., and Chow, V.T. (2011). Excessive neutrophils and neutrophil extracellular traps contribute to acute lung injury of influenza pneumonitis. Am. J. Pathol. *179*, 199–210. https://doi.org/10.1016/j.ajpath.2011.03.013.

Nédélec, Y., Sanz, J., Baharian, G., Szpiech, Z.A., Pacis, A., Dumaine, A., Grenier, J.C., Freiman, A., Sams, A.J., Hebert, S., et al. (2016). Genetic ancestry and natural selection drive population differences in immune responses to pathogens. Cell *167*, 657–669.e21. https://doi.org/10.1016/j.cell.2016.09.025.

O'Brien, K.L., and Finlay, D.K. (2019). Immunometabolism and natural killer cell responses. Nat. Rev. Immunol. *19*, 282–290. https://doi.org/10.1038/s41577-019-0139-2.

Paget, C., Ivanov, S., Fontaine, J., Renneson, J., Blanc, F., Pichavant, M., Dumoutier, L., Ryffel, B., Renauld, J.C., Gosset, P., et al. (2012). Interleukin-22 is produced by invariant natural killer T lymphocytes during influenza A virus infection. J. Biol. Chem. *287*, 8816–8829. https://doi.org/10.1074/jbc.M111.304758.

Peng, H., Jiang, X., Chen, Y., Sojka, D.K., Wei, H., Gao, X., Sun, R., Yokoyama, W.M., and Tian, Z. (2013). Liver-resident NK cells confer adaptive immunity in skin-contact inflammation. J. Clin. Invest. *123*, 1444–1456. https://doi.org/10.1172/JCI66381.

Pernet, E., Downey, J., Vinh, D.C., Powell, W.S., and Divangahi, M. (2019). Leukotriene B4-type I interferon axis regulates macrophage-mediated disease tolerance to influenza infection. Nat. Microbiol. *4*, 1389–1400. https://doi.org/10.1038/s41564-019-0444-3.

Perrone, L.A., Plowden, J.K., García-Sastre, A., Katz, J.M., and Tumpey, T.M. (2008). H5N1 and 1918 pandemic influenza virus infection results in early and excessive infiltration of macrophages and neutrophils in the lungs of mice. PLoS Pathog. *4*, e1000115. https://doi.org/10.1371/journal.ppat.1000115.

Pociask, D.A., Scheller, E.V., Mandalapu, S., McHugh, K.J., Enelow, R.I., Fattman, C.L., Kolls, J.K., and Alcorn, J.F. (2013). IL-22 is essential for lung epithelial repair following influenza infection. Am. J. Pathol. *182*, 1286–1296. https://doi.org/10.1016/j.ajpath.2012.12.007.

Porter, G.A., Jr., and Beutner, G. (2018). Cyclophilin D, somehow a master regulator of mitochondrial function. Biomolecules *8*, 176. https://doi.org/10.3390/biom8040176.

Ritchie, M.E., Phipson, B., Wu, D., Hu, Y., Law, C.W., Shi, W., and Smyth, G.K. (2015). Limma powers differential expression analyses for RNA-sequencing and microarray studies. Nucleic Acids Res. *43*, e47. https://doi.org/10.1093/nar/gkv007.

Robinson, M.D., McCarthy, D.J., and Smyth, G.K. (2010). edgeR: a Bioconductor package for differential expression analysis of digital gene expression data. Bioinformatics *26*, 139–140. https://doi.org/10.1093/bioinformatics/btp616.

Schipke, J., Brandenberger, C., Rajces, A., Manninger, M., Alogna, A., Post, H., and Mühlfeld, C. (2017). Assessment of cardiac fibrosis: a morphometric method comparison for collagen quantification. J. Appl. Phys. *122*, 1019–1030. https://doi.org/10.1152/japplphysiol.00987.2016.

Schneider, D.S., and Ayres, J.S. (2008). Two ways to survive infection: what resistance and tolerance can teach us about treating infectious diseases. Nat. Rev. Immunol. *8*, 889–895. https://doi.org/10.1038/nri2432.

Sengupta, S., Tang, S.Y., Devine, J.C., Anderson, S.T., Nayak, S., Zhang, S.L., Valenzuela, A., Fisher, D.G., Grant, G.R., López, C.B., and FitzGerald, G.A. (2019). Circadian control of lung inflammation in influenza infection. Nat. Commun. *10*, 4107. https://doi.org/10.1038/s41467-019-11400-9.

Shannon, P., Markiel, A., Ozier, O., Baliga, N.S., Wang, J.T., Ramage, D., Amin, N., Schwikowski, B., and Ideker, T. (2003). Cytoscape: a software environment for integrated models of biomolecular interaction networks. Genome Res. *13*, 2498–2504. https://doi.org/10.1101/gr.1239303.

Smith, J.N.P., Zhang, Y., Li, J.J., McCabe, A., Jo, H.J., Maloney, J., and MacNamara, K.C. (2018). Type I IFNs drive hematopoietic stem and progenitor cell collapse via impaired proliferation and increased RIPK1-dependent cell death during shock-like ehrlichial infection. PLoS Pathog. *14*, e1007234. https://doi.org/10.1371/journal.ppat.1007234.

Soares, M.P., Teixeira, L., and Moita, L.F. (2017). Disease tolerance and immunity in host protection against infection. Nat. Rev. Immunol. *17*, 83–96. https://doi.org/10.1038/nri.2016.136.

Sojka, D.K., Plougastel-Douglas, B., Yang, L., Pak-Wittel, M.A., Artyomov, M.N., Ivanova, Y., Zhong, C., Chase, J.M., Rothman, P.B., Yu, J., et al. (2014). Tissue-resident natural killer (NK) cells are cell lineages distinct from thymic and conventional splenic NK cells. Elife *3*, e01659. https://doi.org/10.7554/eLife.01659.

Soneson, C., Love, M.I., and Robinson, M.D. (2015). Differential analyses for RNA-seq: transcript-level estimates improve gene-level inferences. F1000Research *4*, 1521. https://doi.org/10.12688/f1000research.7563.2.

Stegemann-Koniszewski, S., Behrens, S., Boehme, J.D., Hochnadel, I., Riese, P., Guzmán, C.A., Kröger, A., Schreiber, J., Gunzer, M., and Bruder, D. (2018). Respiratory influenza A virus infection triggers local and systemic natural killer cell activation via toll-like receptor 7. Front. Immunol. *9*, 245. https://doi.org/10.3389/fimmu.2018.00245.

Stein-Streilein, J., and Guffee, J. (1986). In vivo treatment of mice and hamsters with antibodies to asialo GM1 increases morbidity and mortality to pulmonary influenza infection. J. Immunol. *136*, 1435–1441.

Storey, J.D., and Tibshirani, R. (2003). Statistical significance for genomewide studies. Proc. Natl. Acad. Sci. U S A *100*, 9440–9445. https://doi.org/10.1073/pnas.1530509100.

Subramanian, A., Tamayo, P., Mootha, V.K., Mukherjee, S., Ebert, B.L., Gillette, M.A., Paulovich, A., Pomeroy, S.L., Golub, T.R., Lander, E.S., and Mesirov, J.P. (2005). Gene set enrichment analysis: a knowledge-based approach for interpreting genome-wide expression profiles. Proc. Natl. Acad. Sci. U S A *102*, 15545–15550. https://doi.org/10.1073/pnas.0506580102.

Talmi-Frank, D., Altboum, Z., Solomonov, I., Udi, Y., Jaitin, D.A., Klepfish, M., David, E., Zhuravlev, A., Keren-Shaul, H., Winter, D.R., et al. (2016). Extracellular matrix proteolysis by MT1-MMP contributes to influenza-related tissue damage and mortality. Cell Host Microbe *20*, 458–470. https://doi.org/10.1016/j.chom.2016.09.005.

Tay, M.Z., Poh, C.M., Rénia, L., MacAry, P.A., and Ng, L.F.P. (2020). The trinity of COVID-19: immunity, inflammation and intervention. Nat. Rev. Immunol. *20*, 363–374. https://doi.org/10.1038/s41577-020-0311-8.

Tzelepis, F., Blagih, J., Khan, N., Gillard, J., Mendonca, L., Roy, D.G., Ma, E.H., Joubert, P., Jones, R.G., and Divangahi, M. (2018). Mitochondrial cyclophilin D regulates T cell metabolic responses and disease tolerance to tuberculosis. Sci. Immunol. *3*, eaar4135. https://doi.org/10.1126/sciimmunol.aar4135.

van Helden, M.J.G., Zaiss, D.M.W., and Sijts, A.J.A.M. (2012). CCR2 defines a distinct population of NK cells and mediates their migration during influenza virus infection in mice. PLoS One *7*, e52027. https://doi.org/10.1371/journal.pone.0052027.

Vaseva, A.V., Marchenko, N.D., Ji, K., Tsirka, S.E., Holzmann, S., and Moll, U.M. (2012). p53 opens the mitochondrial permeability transition pore to trigger necrosis. Cell *149*, 1536–1548. https://doi.org/10.1016/j.cell.2012.05.014.

Vivier, E., Tomasello, E., Baratin, M., Walzer, T., and Ugolini, S. (2008). Functions of natural killer cells. Nat. Immunol. *9*, 503–510. https://doi.org/10.1038/ni1582.

Weiss, I.D., Wald, O., Wald, H., Beider, K., Abraham, M., Galun, E., Nagler, A., and Peled, A. (2010). IFN-gamma treatment at early stages of influenza virus

infection protects mice from death in a NK cell-dependent manner. J. Interferon Cytok. Res. *30*, 439–449. https://doi.org/10.1089/jir.2009.0084.

West, A.P., Shadel, G.S., and Ghosh, S. (2011). Mitochondria in innate immune responses. Nat. Rev. Immunol. *11*, 389–402. https://doi.org/10.1038/nri2975.

Wolk, K., Kunz, S., Asadullah, K., and Sabat, R. (2002). Cutting edge: immune cells as sources and targets of the IL-10 family members? J. Immunol. *168*, 5397–5402. https://doi.org/10.4049/jimmunol.168.11.5397.

Wu, D., Sanin, D.E., Everts, B., Chen, Q., Qiu, J., Buck, M.D., Patterson, A., Smith, A.M., Chang, C.-H., Liu, Z., et al. (2016). Type 1 interferons induce changes in Core metabolism that are critical for immune function. Immunity *44*, 1325–1336. https://doi.org/10.1016/j.immuni.2016.06.006.

Yamashita, M., and Passegue, E. (2019). TNF-alpha coordinates hematopoietic stem cell survival and myeloid regeneration. Cell Stem Cell *25*, 357–372.e7. https://doi.org/10.1016/j.stem.2019.05.019.

Yanai, H., Budovsky, A., Tacutu, R., Barzilay, T., Abramovich, A., Ziesche, R., and Fraifeld, V.E. (2016). Tissue repair genes: the TiRe database and its implication for skin wound healing. Oncotarget *7*, 21145–21155. https://doi.org/10.18632/oncotarget.8501.

Yang, C., Tsaih, S.W., Lemke, A., Flister, M.J., Thakar, M.S., and Malarkannan, S. (2018). mTORC1 and mTORC2 differentially promote natural killer cell development. Elife *7*, e35619. https://doi.org/10.7554/eLife.35619.

Zenewicz, L.A., Yancopoulos, G.D., Valenzuela, D.M., Murphy, A.J., Stevens, S., and Flavell, R.A. (2008). Innate and adaptive interleukin-22 protects mice from inflammatory bowel disease. Immunity *29*, 947–957. https://doi.org/10.1016/j.immuni.2008.11.003.

Zhang, T., Liu, S., Yang, P., Han, C., Wang, J., Liu, J., Han, Y., Yu, Y., and Cao, X. (2009). Fibronectin maintains survival of mouse natural killer (NK) cells via CD11b/Src/β-catenin pathway. Blood *114*, 4081–4088. https://doi.org/10.1182/blood-2009-05-219881.

Zhao, X., Khan, N., Gan, H., Tzelepis, F., Nishimura, T., Park, S.Y., Divangahi, M., and Remold, H.G. (2017). Bcl-xL mediates RIPK3-dependent necrosis in M. tuberculosis-infected macrophages. Mucosal Immunol. *10*, 1553–1568. https://doi.org/10.1038/mi.2017.12.

STAR★METHODS

KEY RESOURCES TABLE

REAGENT or RESOURCE	SOURCE	IDENTIFIER
Antibodies		
Fixable Viability Dye eFluor506	eBioscience	Cat#65-0863-18
anti-CD16/32 (clone 93)	eBioscience	RRID: AB_467134
anti-Ter-119 biotin-conjugated (clone Ter119)	BD Biosciences	RRID: AB_394985
anti-CD11b biotin-conjugated (clone M1/70)	BD Biosciences	RRID: AB_394773
anti-CD5 biotin-conjugated (clone 53-7.3)	BD Biosciences	RRID: AB_394557
anti-CD4 biotin-conjugated (clone RM4-5)	BD Biosciences	RRID: AB_394581
anti-CD8a biotin-conjugated (clone 53-6.7)	BD Biosciences	RRID: AB_394567
anti-CD45R biotin-conjugated (clone RA3-6B2)	BD Biosciences	RRID: AB_394641
anti-Ly6G/C biotin-conjugated (clone RB6-8C5)	BD Biosciences	RRID: AB_394641
Streptavidin-APC-Cy7	eBioscience	RRID: AB_10366688
anti-c-Kit-APC (clone 2B8)	BD Biosciences	RRID: AB_2739664
anti-Sca-1-PE-Cy7 (clone D7)	eBioscience	RRID: AB_469668
anti-CD34-FITC (clone RAM34)	eBioscience	RRID: AB_465020
Anti-CD16/32-PerCP-eFluor710 (clone 93)	eBioscience	RRID: AB_996659
Anti-CD122-PE-CF594 (Clone TM-β1)	BD Biosciences	RRID:AB_2738936
Anti-CD244.2-BUV395 (Clone 2B4)	BD Biosciences	RRID:AB_2739974
Anti-CD127-BV786 (Clone SB/199)	BD Biosciences	RRID:AB_2738403
Anti-CD27-FITC (Clone LG.3A10)	BioLegend	RRID:AB_1236466
Anti-IFN-γ-APC (Clone XMG1.2)	BD Biosciences	RRID:AB_398551
Anti-IL-22-PE (Clone 1H8PWSR)	eBioscience	RRID:AB_10597428
Anti-p53-PE	BD Biosciences	RRID:AB_396557
Anti-Ki67-APC (Clone SolA15)	eBioscience	RRID:AB_2688057
Anti-Perforin-APC (Clone S16009A)	BioLegend	RRID:AB_2721463
Anti-Active Caspase 3-PE (Clone C92-605)	BD Biosciences	RRID:AB_2033931
Anti-granzyme B-PE (Clone GB11)	eBioscience	RRID:AB_1659718
Anti-SiglecF-PE-CF594 (Clone E50-2440)	BD Biosciences	RRID: AB_2687994
Anti-CD11b-BUV395 (Clone M1/70)	BD Biosciences	RRID:AB_2738276
Anti-Ly6G-PerCP-eFluor710 (Clone 1A8)	eBioscience	RRID: AB_2573892
Anti-Ly6G-AlexaFluor700 (Clone RB6-8C5)	eBioscience	RRID: AB_10611860
Anti-Ly6C-FITC (Clone AL-21)	BD Biosciences	RRID: AB_394628
Anti-Ly6C-APC (Clone HK1.4)	eBioscience	RRID: AB_1724153
Anti-F4/80-APC-eFluor780 (Clone BM8)	eBioscience	RRID:AB_2637188
Anti-CD11c-BV421	BD Biosciences	RRID:AB_2744278
Anti-CD45.2-BUV395 (Clone 104)	BD Biosciences	Cat# 564,616
Anti-CD45.2-FITC (Clone 104)	BD Biosciences	RRID:AB_395041
Anti-CD45.1-APC (Clone A20)	BD Biosciences	RRID: AB_1645214
Anti-CD3e-PE-Cy7 (Clone 145-2C11)	BD Biosciences	RRID:AB_394460
Anti-NKp46-BUV737 (Clone 29A1.4)	BD Biosciences	RRID:AB_2870131
Anti-NKp46-APC (Clone 9E2/NKp46)	BD Biosciences	RRID:AB_398653
Anti-CD49b-BV421 (Clone DX5)	BD Biosciences	RRID:AB_2737983

(*Continued on next page*)

Continued

REAGENT or RESOURCE	SOURCE	IDENTIFIER
Anti-CD49a-PE (Clone Ha31/8)	BD Biosciences	RRID:AB_11153117
Anti-CD27-PE-Cy7 (Clone LG.3A10)	BD Biosciences	RRID:AB_2738309
MitoTracker Green FM	Invitrogen	Cat#M7514
MitoTracker Orange CMTMRos	Invitrogen	Cat#M7510
MitoSOX Red	Invitrogen	Cat#M36008
Viability NucSpot Far-Red	Biotium	Cat#40085
PE Annexin V Apoptosis Detection Kit with 7-AAD	BioLegend	Cat# 640,934
Goat Anti-rabbit-Alexa Fluor 555	Invitrogen	Cat# A32732
Anti-CYPD	Abcam	Cat# AB110324
Anti GAPDH	Millipore	Cat# AB2302
Bacterial and virus strains		
Mouse-adapted influenza A/Puerto Rico/8/34 (H1N1) virus	Gift from Dr. Jonathan McCullers	N/A
Chemicals, peptides, and recombinant proteins		
Enrofloxacin, Baytril 50mg/mL	Bayer	DIN 02169428
RPMI-1640 with L-glutamine	Wisent	Cat#350-000CL
BSA	Wisent	Cat#800-195-EG
Fetal Bovine Serum	Wisent	Cat#80150
Penicillin/Streptomycin	Wisent	Cat#450-115-EL
Collagenase IV	Sigma	Cat#5138
Paraformaldehyde 16%	ThermoFisher	Cat#28908
RNeasy Kit	Qiagen	Cat# NC9677589
5x RT MasterMix	ABM	Cat#G592
EvaGreen qPCR MasterMix	ABM	Cat#ABMMastermix-S
TPCK Trypsin	ThermoFisher	Cat#20233
DMEM	Gibco	Cat#11965-092
Tween 20	Sigma	Cat# P7949
Triton X-100	Sigma	Cat# T9284
10% Formalin	Sigma	HT501128
NaCl	Fisher	Cat# S6713
HEPES	Wisent	Cat# 330-050-EL
Glycerol	Wisent	Cat# 800-040-LL
1mM EDTA	Sigma	Cat# E7889
Protease inhibitor tablets	Roche	Cat# 11,697,498,001
Phosphotase inhibitor tablets	Roche	Cat# 4,906,845,001
L-Glutamine	Sigma	Cat# 59202C
Minimum Essential Media Powder	Gibco	Cat# 61,100,103
10,000 MW Texas Red Dextran	Invitrogen	Cat# D1828
Phosphate Buffered Saline	Wisent	Cat# 311-010-CL
Recombinant Murine IL-22	Peprotech	Cat# 210-22
Recombinant Murine IFN-γ	Peprotech	Cat# 315-05
Dextrose	ThermoFisher	Cat# D16-10
Sodium Pyruvate	Sigma	Cat# S8636
Recombinant murine IL-12	Biolegend	Cat# 577,004
Ultraleaf anti-mouse IL-4	Biolegend	Cat# 504,122
Recombinant human TGF-β	Biolegend	Cat# 781,804
Recombinant murine IL-23	Biolegend	Cat# 589,002
Recombinant murine IL-6	Biolegend	Cat# 575,706
Recombinant murine IL-18	Biolegend	Cat# 767,006

(*Continued on next page*)

Continued

REAGENT or RESOURCE	SOURCE	IDENTIFIER
Critical commercial assays		
Verikine IFN-β ELISA	PBL Assay Science	Cat# 42,400–1
IFN-γ ELISA	R&D Systems	Cat# DY485-05
IL-22 ELISA	R&D Systems	Cat# DY582-05
CytoTox 96 Non-Radioactive Cytotoxicity Assay	Promega	Cat# G1780
EasySep Mouse NK Cell Isolation Kit	Stem Cell Technologies	Cat# 19,855
BCA Protein Assay Kit	ThermoFisher	Cat# PI23225
Clarity ECL Kit	Bio-Rad	Cat# #1705061
Protein Transport Inhibitor with Brefeldin A	BD Biosciences	Cat# 555,029
Cell Activation Cocktail	BioLegend	Cat# 423,303
Cytofix/Cytoperm Kit	BD Biosciences	Cat# BDB554714
Seahorse MitoStress Test Kit	Agilent	Cat# 103,015-100
EasySep Mouse T cell Isolation Kit	Stem Cell Technologies	Cat# 19851
Mouse T-Activator CD3/CD28 Dynabeads	Gibco	Cat# 11452D
Deposited data		
Bulk RNA-Seq Data	GEO: GSE163290	
Processed Bulk RNA-Seq Data	https://doi.org/10.5281/zenodo.4300712	
Code for RNA-Seq analysis	https://doi.org/10.5281/zenodo.4300712	
Experimental models: Cell lines		
MDCK	ATCC	Cat#CRL-2936
B16-Blue IFN-α/β	InvivoGen	Cat#bb-ifnt1
Experimental models: Organisms/strains		
Mouse: C57Bl/6J	The Jackson Laboratory	IMSR Cat# JAX:000,664, RRID: IMSR_JAX:000,664
Mouse CD45.1 + B6. SJL-Ptprca Pepcb/BoyJ	The Jackson Laboratory	IMSR cat# JAX:002,014, RRID: IMSR_JAX:002,014
Mouse: B6.129S7-Ifngr1tm1Agt/J	The Jackson Laboratory	MSR Cat# JAX:003,288, RRID: IMSR_JAX:003,288
Mouse: *Il22*$^{-/-}$	Gift from Dr. Irah King	N/A
Software and algorithms		
Graphpad Prism version 9	GraphPad	SCR_015,807
FACSDiva Software	BD Biosciences	SCR_001,456
FlowJo software v.10	Tree Star	SCR_000,410
Trim Galore v0.6.2, Cutadapt v2.2	Martin (2011)	http://www.bioinformatics.babraham.ac.uk/projects/trim_galore/
Kallisto (v0.43)	Bray et al. (2016)	N/A
R (v3.6.3)	Soneson et al. (2015)	N/A
edgeR (v3.26.8)	Robinson et al. (2010)	SCR_012,802
limma (v3.40.6)	Ritchie et al. (2015)	SCR_010,943
CLUEGO	Bindea et al. (2009)	SCR_005,748
ImageJ	NIH	http://imagej/net/software/fiji
AperioImageScope	Leica	https://www.leicabiosystems.com/digital-pathology/manage/aperio-imagescope/
ZEISS ZEN 2.3 Pro	Zeiss	https://www.zeiss.com/microscopy/int/
Wave Desktop 2.3	Agilent Technologies	N/A
Other		
PVDF Membranes	Bio-Rad	Cat# #1620177

RESOURCE AVAILABILITY

Lead contact

Further information and requests for resources and reagents should be directed to and will be fulfilled by the Lead Contact, Maziar Divangahi (maziar.divangahi@mcgill.ca).

Materials availability

No unique reagents were generated for this study.

Data and code availability

- RNA-Seq data have been deposited at a GEO database and are publicly available as of the date of publication. DOIs are listed in the key resources table.
- All original code has been deposited at Zenodo and is publicly available as of the date of publication. DOIs are listed in the key resources table.
- Any additional information required to reanalyze the data reported in this paper is available from the lead contact upon request.

EXPERIMENTAL MODEL AND SUBJECT DETAILS

Mice

Six- to ten-week-old C57BL/6, CD45.1 and *Ifngr*$^{-/-}$ mice were purchased from Jackson Laboratories. *CypD*$^{-/-}$ mice were provided by M. Forte (Oregon Health and Science University, Portland, OR, USA). Littermates were generated by backcrossing C57BL/6 and *CypD*$^{-/-}$ and then breeding subsequent heterozygotes. All animals were housed and inbred at the animal facility of the Research Institute of McGill University under SPF conditions and *ad libitum* access to food and water. Experiments were performed using age- and sex-matched mice that were randomly assigned to groups.

Ethics

All experiments involving animals were approved by McGill University (permit number 2010–5860) in strict accordance with the guidelines set out by the Canadian Council on Animal Care.

METHOD DETAILS

Viruses & infection

All *in vivo* infections were performed using mouse adapted influenza A/Puerto Rico/8/34 (H1N1) virus (IAV), kindly provided by Dr. Jonathan A. McCullers (St. Jude Children Research Hospital). Mice were challenged intranasally (in 25μL PBS) with IAV at a sublethal dose of 50 PFU or a lethal dose (LD_{50}) of 90 PFU. 90 PFU was used for the survival experiments in Figures 1A, S1E and 7F. For all other experiments, 50 PFU was used. During survival experiments mice were monitored twice daily for signs of duress and weighed daily. Mice reaching 75% of original body weight were considered moribund and sacrificed. Viruses were propagated and isolated from Madin-Darby Canine Kidney (MDCK) cells and titrated using standard MDCK plaque assays. MDCK cells were obtained from the American Type Culture Collection and maintained in Dulbecco's modified Eagle medium enriched with 10% (*v*/*v*) FBS and 100 U ml^{-1} penicillin/streptomycin. Viral titers were determined in lung homogenates (homogenized in 500 μL PBS) using standard MDCK plaque assays.

In vivo methods

Generation of chimeric mice

CD45.1^{+} B6 mice or *CypD*$^{-/-}$ mice were lethally irradiated with 9 Gy following 3 days of antibiotic treatment (0.5g Enrofloxacin (Bayer) per liter of drinking water). 16 hours later, the BM compartment was reconstituted with 4x10^{6} nucleated cells from either CD45.1^{+} mice (*CypD*$^{-/-}$ recipient) or *CypD*$^{-/-}$ mice (CD45.1^{+} recipient) and antibiotic treatment was maintained for 2 additional weeks. Between 10 and 12 weeks post-injection, reconstitution was validated by flow cytometry and was >90%. Mice were then infected for downstream assays.

Texas red-dextran lung permeability

WT and *CypD*$^{-/-}$ mice were infected for 7 days with 50 PFU. On day 7, mice were delivered 25μL of 50mg/mL (1.25mg) Texas Red-Dextran (10,000 MW) intranasally. 1 h later mice were sacrificed and lungs were carefully excised without damaging. Lungs were imaged using the In Vivo Xtreme (Bruker) using fluorescence capture. Resulting images were then analyzed for total fluorescent intensity of lung images using ImageJ software (National Institutes of Health). During the 1 h of incubation Texas Red-Dextran molecules diffused into the blood of infected mice, due to the loss of epithelial/endothelial barrier integrity. Therefore, lower fluorescence is indicative of increased damage and compromised barrier integrity.

IL-22 or IFN-γ treatment

Recombinant murine IL-22 or IFN-γ was purchased from Peprotech. Mice were intranasally infected with 50 PFU of IAV. On day 5 post-infection, mice were given either PBS, IL-22 or IFN-γ (both 100ng/25μL) intranasally. Mice were sacrificed on day 7 post-infection, and the lungs were harvested and processed to determine the pulmonary viral load, or the BAL collected for damage assays. In some experiments, mice were infected with 90 PFU and IL-22 was delivered as stated and survival was monitored.

Adoptive transfer model

NK cells were purified from uninfected spleens of WT, *CypD*$^{-/-}$ and *Il22*$^{-/-}$ mice using the EasySep Mouse NK Cell Isolation Kit (Stem Cell Technologies) according to the supplier's recommendations. Sorted cells were counted, washed (cold sterile PBS) and normalized to 1x10^5 cells/50μL of sterile PBS. Purity was verified by flow cytometry and purity was always over 85% NK cells prior to transfer. NK cells were then transferred into *Il22*$^{-/-}$ or *CypD*$^{-/-}$ mice on day 5 post-infection (50 PFU) via the intratracheal route. 2 days later, BAL were harvested for damage assays and lungs were harvested for viral load analysis or histology.

Ex Vivo experiments

Protein in the BAL

BAL were collected by cannulating the trachea with a 22-gauge cannula, then washing the lungs with 3 × 1 mL of cold, sterile PBS. The total volume recovered after lavage was ~0.7 mL. Samples were spun down (1,500 r.p.m.; 10 min) and the total protein content was assessed by Pierce BCA Protein assay (Thermo Fisher Scientific).

Extracellular flux analysis

Real-time oxygen consumption rates (OCR) of purified splenic NK cells were measured in XF media (non-buffered DMEM containing 2mM L-glutamine, 25mM glucose and 1mM sodium pyruvate) using a Seahorse XFe 96 Analyzer (Agilent Technologies). For the mitochondrial stress test, mitochondrial inhibitors oligomycin, fluorocarbonyl cyanide phenylhydrazone (FCCP), antimycin A and rotenone were used, as per the manufacturer's recommendations. Briefly, NK cells were seeded at a density of 200,000 cells per well and 3 basal measurements were taken. Following this, 2 consecutive measurements were taken following each injection of oligomycin, FCCP, and antimycin A with rotenone. All measurements were normalized to cell number using a crystal violet dye extraction assay. Oxygen consumption curves were generated using Wave Desktop 2.3 (Agilent Technologies). Basal OCR was calculated by subtracting measurement 7 (non-mitochondrial respiration) from measurement 1. Maximal respiration was calculated by subtracting measurement 7 (non-mitochondrial respiration) from measurement 5 and spare respiratory capacity was the difference between maximal respiration and basal rate.

Flow cytometry

Lung tissues were perfused with 10 mL of PBS, harvested and minced before collagenase digestion (150 U mL^{-1}) for 1 h at 37°C. Lungs were crushed through a 40 μm nylon mesh, and red blood cells were lysed. For bone marrow staining, cells were isolated following aseptic flushing of the tibiae and femurs, and red blood cells were lysed. BAL were collected as previously described, spun down and red blood cells lysed. Spleens were aseptically removed, crushed through a 40 μm nylon mesh, and red blood cells were lysed. Then total cell counts were determined with a hemocytometer. In some experiments BAL were counted prior to red blood cell lysis to enumerate erythrocyte influx into the airways and then red blood cells were lysed. For peripheral blood staining, the blood was collected by cardiac puncture in a BD Microtainer tube and stained extracellularly; red blood cells were then lysed.

Cells were initially stained with eFluor-506 viability dye in PBS (eBioscience; 20 min; 4°C), washed and surface stained with anti-CD16/32 (BD Biosciences; Clone: 2.4G2) in 0.5% BSA/PBS solution to block non-specific antibody interactions with Fc receptors (10 min; 4°C). Cells were then surface stained with combinations of PE-CF594-conjugated anti-SiglecF (Clone: E50-2440), BUV395-conjugated anti-CD11b (Clone: M1/70), PerCP-eFluor710-or AlexaFluor700-conjugated anti-Ly6G (Clone: 1A8 or RB6-8C5, respectively), fluorescein isothiocyanate (FITC)- or allophycocyanin (APC)-conjugated anti-Ly6C (Clone: AL-21 or HK1.4, respectively), APC-eFluor780-conjugated anti-F4/80 (Clone: BM8), BV421-conjugated anti-CD11c (Clone: N418), FITC- or BUV395-conjugated anti-CD45.2 (Clone: 104) or APC-conjugated anti-CD45.1 (Clone: A20), Pe-Cy7-conjugated anti-CD3e (Clone: 145-2C11), BV786-conjugated anti-CD127 (Clone: SB/199), APC- or BUV737-conjugated anti-NKp46 (Clone: 9E2/NKp46 or 29A1.4, respectively), BV421-conjugated anti-CD49b (Clone: DX5), PE-conjugated anti-CD49a (Clone: Ha31/8) (all from BD BioScience, except PerCP-efluor710-conjugated anti-Ly6G and APC-eFluor780-conjugated F4/80 from eBioscience), or PE-Cy7-conjugated (BD Biosciences) or FITC-conjugated (eBioscience) anti-CD27 (Clone: LG.3A10). Cells were then fixed with 1% PFA for 1 h, washed and acquired in 0.5% BSA/PBS solution.

In some experiments, following extracellular staining, samples were stained intracellularly for Ki67, active Caspase 3, perforin, granzyme B or p53. For APC-conjugated anti-Ki67 (Clone: SolA15, eBioscience), or APC-conjugated anti-perforin (Clone: S16009A, Biolegend) and PE-conjugated anti-active Caspase 3 (Clone: C92-605, BD Biosciences), or anti-granzyme B (Clone: GB11, eBioscience) cells were initially fixed and permeabilized using BD Cytofix/Cytoperm (BD Biosciences) for 30 min at 4°C and then stained for 1 h. Cells were washed and acquired. For p53 staining, cells were initially fixed and permeabilized for 1 h using the Foxp3/Transcription Factor Staining Buffer Set (eBioscience) and then stained using the PE-conjugated anti-p53 Set (Catalog No: 557,027, BD Biosciences), according to the manufacturer's instructions. The provided PE-conjugated isotype was used as a control.

In experiments involving bone marrow progenitors, cells were processed, counted, stained for viability and blocked as before. Cells were then stained with biotin conjugated anti-Ly6C/G (Clone: RB6-8C5), anti-CD5 (Clone: 53-7.3), anti-B220 (Clone:

RA3-6B2), anti-Ter119 (Clone: Ter119), anti-CD4 (Clone: RM4-4) and anti-CD8 (Clone: 53-6.7) for 20 min at 4°C. Cells were then washed and stained with APC-Cy7-conjugated streptavidin, APC-conjugated anti-cKit (Clone: 2B8), PE-Cy7-conjugated Sca-1 (Clone: D7) for LKS cells. For CMP/GMP experiments, cells were not blocked and instead FITC-conjugated anti-CD34 (Clone: RAM34) and PerCP-eFluor710-conjugated anti-CD16/32 (all from BD Biosciences, except anti-CD16/32, anti-c-Kit and anti-Sca-1-PE-Cy7 from eBioscience) were added to the previous cocktail. For NK cell progenitors, PE-CF594-conjugated anti-CD122 (Clone: TM-β1) and BUV395-conjugated anti-CD244.2 (Clone: 2B4) were added along with FITC-conjugated anti-CD27 (Clone: LG.3A10) (BioLegend) and BV786-conjugated anti-CD127 (Clone: SB/199) (BD Biosciences) as previously described.

Finally, for experiments involving intracellular cytokine staining (ICS), $2x10^6$ single splenocytes or BAL cells were incubated for 4 h at 37°C in the presence of PMA/Ionomycin and Brefeldin A (Cell Activation Cocktail; BioLegend) or GolgiPlug (BD Biosciences). Cells were then stained extracellularly, fixed and permeabilized using BD Cytofix/Cytoperm (BD Biosciences), before being stained intracellularly for PE-conjugated anti-IL-22 (Clone: 1H8PWSR, eBioscience) and APC-conjugated anti-IFN-γ (Clone: XMG1.2, BD Biosciences).

Flow cytometry acquisition was performed using BD LSRFortessa X-20 (BD Biosciences) with FACSDiva Software version 8.0.1 (BD Biosciences). Analysis was performed using FlowJo software version 10 (Tree Star).

Evaluation of mitochondrial fitness using mitotracker green/orange and mitosox red

Single cell suspensions were stained with extracellular antibodies as described above and then with Mitotracker Green and Orange 150nM, or MitoSox Red 1μM (Invitrogen technologies) in PBS for 30 min at room temperature and then washed with PBS. For experiments involving mitochondrial potential, dysregulated mitochondria were Mitotracker Green^{hi} and Mitotracker Orange^{lo}, while respiring mitochondria were considered as Mitotracker Green^{hi} and Mitotracker Orange^{hi} as previously described (Ip et al., 2017)

Western blot

500,000 NK cells were isolated from WT and *CypD*$^{-/-}$ spleens using EasySep Mouse NK Cell Isolation Kit (Stem Cell Technologies) according to the supplier's recommendations. Cells were lysed in lysis buffer (1% Triton X-100, 150mM NaCl, 20mM HEPES pH7.5, 10% glycerol, 1mM EDTA, supplemented with anti-protease and anti-phosphatase cocktails, Roche) and protein concentration was determined using a BCA assay (Pierce). 10 μg of protein were resolved by SDS-PAGE and transferred onto PVDF membranes (Biorad). Membranes were blocked and incubated overnight at 4°C with gentle agitation with primary antibodies. The following primary antibodies were used: anti-CYPD (1:1000, Abcam), anti-GAPDH (1:1000, Millipore). Primary antibodies were followed by HRP-conjugated secondary antibodies and signal was detected using Clarity ECL kit (Biorad) and acquired on Chemidoc MP System (Biorad).

Immunofluorescence

50,000 NK cells were isolated from WT and *CypD*$^{-/-}$ spleens using EasySep Mouse NK Cell Isolation Kit (Stem Cell Technologies) according to the supplier's recommendations and seeded in polylysine-treated microscopy slides. Cells were then stained with Mitotracker Green (100nM, Invitrogen) for 30 min at 37°C and fixed in 4% (*v*:*v*) paraformaldehyde for 15 min. Cells were then permeabilized by incubating with 0.1% Triton X-100 in PBS for 15 min. Samples were blocked with 1% milk in PBS Tween 0.1% for 1 h, then incubated with anti-CYPD (Abcam) overnight at 4°C. Cells were incubated for 1 h with secondary antibody Alexa Fluor 555-conjugated goat anti-rabbit (1:1,000; Invitrogen). Coverslips were mounted (ProLong Diamond Antifade; Invitrogen) onto microscope slides. Images were acquired using a Zeiss LSM 700 laser-scanning confocal microscope.

T and NK cell stimulation

T and NK cells were purified from the spleens of naive WT and *CypD*$^{-/-}$ mice using the EasySep Mouse T cell Isolation Kit and EasySep NK cell Isolation Kit respectively (Stem Cell Technologies). Isolated cells were counted and resuspended at 4 x 10^6/mL in pre-warmed culture media (Roswell Park Memorial Institute media enriched with 10% FBS, 2 mM L-glutamine, 100 U ml−1 penicillin/streptomycin and 25mM HEPES). T cells were activated with Mouse T-Activator CD3/CD28 Dynabeads (Gibco) in a 1:1 bead to cell ratio and a cocktail of cytokines and blocking antibodies (all from Biolegend). For T_H1 polarization conditions, rmIL-12 (20 ng/mL) + αIL-4 (10 μg/mL) was used, and for T_H17 polarization rhTGF-β1 (2 ng/mL) + rmIL-6 (25 ng/mL) + αIL-4 (10 μg/mL) + rmIL23 (20ng/mL). 50μl of cells with 50μl of stimulation mix were plated on a 96-well plate and incubated at 37°C. After 3 days of culture, T cells were reactivated with PMA (50 ng/mL) and ionomycin (500 ng/mL) for 4 h. NK cells were plated in the same manner, and stimulated with rmIL-18 (50ng/mL) and rmIL-23 (20ng/mL) (both from Biolegend) for 18 h at 37°C. The supernatants were collected for downstream analyses.

Histopathological analysis

Lungs were inflated with and fixed for 48 h in 10% formalin, then embedded in paraffin. Next, 5 μm sections were cut and stained with Haematoxylin and Eosin or Masson's Trichrome. Slides were scanned at a resolution of 20× magnification and pictures were taken using a Leica Aperio slide scanner (Leica). Quantification of collagen-afflicted areas on Masson's Trichrome stained slides was performed using ImageJ software (National Institutes of Health) as previously described (Schipke et al., 2017).

Total bioactive IFN-I assay

Secretion of total active IFN-I (both IFN-α and IFN-β) in BAL and lung homogenates was assessed using the B16-Blue IFN-α/-β reporter cell line for murine samples (from InvivoGen), according to the specifications of the manufacturer. B16 cells were maintained in RPMI supplemented with 10% (*v*/*v*) FBS and 100 U ml^{-1} penicillin/streptomycin.

Cell death analysis

Lactate dehydrogenase release in the BAL of IAV-infected mice was quantified using the CytoTox 96 Non-Radioactive Cytotoxicity Assay (Promega), per the manufacturer's recommendations. Dead cell levels were assessed using PE-AnnexinV (BioLegend) and

NucSpot Far-Red (Biotium), according to the manufacturer's instructions and unfixed cells were acquired immediately by flow cytometry.

Wet-to-dry ratio

Lungs were harvested from naive or IAV-infected mice (50 PFU; day 7 post-infection), and blood clots were carefully removed. Then, the lungs were weighed (wet weight) and dried in an oven (56°C, 2 d; dry weight), and the dry weight was measured. Data are presented as the ratio of wet weight to dry weight.

ELISA

IFN-β levels in infected lungs and BAL were measured using a VeriKine Mouse IFN-β ELISA kit (PBL Assay Science). IFN-γ and IL-22 levels were assessed by ELISA (R&D Systems), as directed by the manufacturer.

RNA isolation and reverse transcription quantitative PCR (qPCR)

RNA from purified NK cells was extracted using RNeasy Kit (Qiagen) according to the manufacturer's instructions. Some 500 ng of RNA were reverse transcribed using the ABM 5X RT MasterMix (Applied Biological Materials), as directed by the manufacturer. cDNA was generated by qPCR using EvaGreen (Applied Biological Materials). Cq values obtained on a CFX96 PCR System (Bio-Rad) were analyzed using $2^{-\Delta Cq}$ formula normalizing target gene expression to *Gapdh*.

Bulk RNA-Seq library preparation and RNA-sequencing

Bulk RNA was collected from purified splenic NK cells from 5 WT (1 control, 4 IAV-infected) and 5 *CypD*$^{-/-}$ mice (1 control, 4 IAV-infected). Sequencing libraries were constructed using the the Illumina TruSeq protocol. Libraries were sequenced on an Illumina NovaSeq (paired-end 100 base pair) to an average depth of 42.6 million reads per sample. Adapter sequences and low-quality score bases were trimmed from reads using Trim Galore (v0.6.2, Cutadapt v2.2) (Martin, 2011) in paired-end mode (-q 20 –paired –phred33). Trimmed reads were pseudoaligned to the *Mus musculus* reference transcriptome (mm10.81, downloaded from Ensembl) using the quant function in kallisto (v0.43) (Bray et al., 2016) in paired-end mode (average of 24.7 million pseudoaligned reads per sample). Gene-level expression estimates accounting for the average transcript length across samples were calculated using the R (v3.6.3) package tximport (v1.14.2) (Soneson et al., 2015).

QUANTIFICATION AND STATISTICAL ANALYSIS

Statistical analysis for mouse work

Data are presented as means ± s.e.m. Statistical analyses were performed using GraphPad Prism version 8.0.2 software (GraphPad). Statistical differences were determined using a two-sided log rank test (survival studies), one-way analysis of variance (ANOVA) followed by Sidak's multiple comparisons test, two-way ANOVA followed by Dunnett's or Tukey's multiple comparisons test, or two-tailed Student's T Test, as outlined in the Figure Legends. Significance is denoted by *p < 0.05, **p < 0.01, ***p < 0.001, ****p < 0.0001.

Modeling the effect of the *CypD*$^{-/-}$ genotype on gene expression

Expression data was filtered for protein-coding genes that were sufficiently expressed across all samples (median logCPM >1), leaving 12,451 genes for downstream analysis. After removing non-coding and lowly-expressed genes, normalization factors to scale the raw library sizes were calculated using calcNormFactors in edgeR (v3.26.8) (Robinson et al., 2010). The voomWithQualityWeights function in limma (v3.40.6) (Ritchie et al., 2015) was used to apply these size factors, estimate the mean-variance relationship, convert counts to logCPM values, and estimate sample-specific observational weights that take into account variation in sample quality.

The following nested linear model was used to identify genes for which expression levels are differentially-expressed between WT and *CypD*$^{-/-}$ mice within each condition:

$$\mathrm{M}_1 : E(i,j) \sim \begin{cases} \beta_0(i) + \beta^{ctl}_{CypD}(i) \cdot CypD(j) + \beta_{M\_aligned}(i) \cdot M\_aligned(j) + \varepsilon^{ctl}(i,j) \; if \; \text{Condition} = ctl \\ \beta_0(i) + \beta_{flu}(i) + \beta^{flu}_{CypD}(i) \cdot CypD(j) + \beta_{M\_aligned}(i) \cdot M\_aligned(j) + \varepsilon^{flu}(i,j) \; \text{if Condition} = flu \end{cases}$$

Here, $E(i,j)$ represents the expression estimate of gene *i* for individual *j*, is the global intercept accounting for the expected expression of gene *i* in a control WT mouse, $\beta^{ctl}_{CypD}(i)$ and $\beta^{flu}_{CypD}(i)$ indicate the effects of the *CypD*$^{-/-}$ genotype on gene *i* within each condition, and $\beta_{flu}(i)$ represents the intrinsic infection effect of IAV infection. Further, *M_aligned* represents the mean-centered, scaled (mean = 0, standard deviation = 1) number of pseudoaligned reads per sample (in millions), with $\beta_{M\_aligned}$ being the impact of read depth on expression. Finally, ε^{cdt} represents the residuals for each respective condition (*ctl* or *flu*) for each gene *i*, individual *j* pair. The model was fit using the lmFit and eBayes functions in limma, and the estimates of the genotype effect ($\beta^{ctl}_{CypD}(i)$ and $\beta^{flu}_{CypD}(i)$) were extracted across all genes, along with their corresponding p values. These estimates represent the genotype-related (WT vs *CypD*$^{-/-}$) differential expression effects within each condition. We controlled for false discovery rate (FDR) using an approach analogous to that of Storey and Tibshirani (Nedelec et al., 2016; Storey and Tibshirani, 2003), which derives the null distribution empirically. To obtain a null, we performed 10 permutations, where genotype label (WT or *CypD*$^{-/-}$) was permuted within infection condition (control or IAV-infected). We considered genes significantly differentially-expressed between genotypes if they had a β^{ctl}_{CypD} or β^{flu}_{CypD} |

logFC| > 0.5 and an FDR <0.10. Of note, all of our downstream analyses focused only on the *CypD*$^{-/-}$ effect in the IAV-infected condition (β^{flu}_{CypD}).

Gene set enrichment analyses

Gene set enrichment analysis was performed using two independent methods, fgsea (Korotkevich et al., 2019) and ClueGO (Bindea et al., 2009), depending on the type of data being evaluated. The enrichment program specifications and the data in which they were used to assess enrichments are described below:

The R package fgsea (v1.10.1) was used to perform gene set enrichment analysis for the genotype effects using the H hallmark gene sets (Subramanian et al., 2005). Input t-statistics were obtained directly from the topTable function in limma. These t-statistics were then ranked and used to perform the enrichment tests with the following parameters: minSize = 15, maxSize = 500, nperm = 100,000. Enrichments scores (ES) and Benjamini-Hochberg adjusted p values output by fgsea were collected for each tested gene set.

Gene set enrichment analysis was also performed for our lists of differentially-expressed (DE) genes between the WT and *CypD*$^{-/-}$ mice in the influenza-infected condition using the ClueGO (v2.5.7) (Bindea et al., 2009) Cytoscape (v3.7.1) (Shannon et al., 2003) module in functional analysis mode, where the target set of genes was either the list of genes showing higher expression in the WT or *CypD*$^{-/-}$ mice and the background set was the list of all genes tested. Specifically, we tested for the enrichment of GO terms related to biological processes (ontology source: GO_BiologicalProcess-EBI-UniProt-GOA-ACAP-ARAP_08.05.2020_00h00) using the following parameters: visual style = Groups, default Network Specificity, no GO Term Fusion, min. GO Tree Interval level = 3, max. GO Tree Interval level = 8, min. number of genes = 2, min. percentage of genes = 4.0, statistical test used = Enrichment (right-sided hypergeometric test), p value correction = Benjamini-Hochberg. For the graphical representation of the enrichment analysis, ClueGO clustering functionality was used (kappa threshold score for considering or rejecting term-to-term links set to 0.4). Only pathways with an FDR <0.01 are reported.

To test for an enrichment of WT or *CypD*$^{-/-}$ DE genes in the IAV-infected condition among genes known to be involved in tissue repair and wound healing (TiRe gene set, curated from Yanai et al. (Yanai et al., 2016), n = 220 retained in our dataset), we calculated the proportion in our WT or *CypD*$^{-/-}$ DE gene lists that also fall into the TiRe gene set and considered this our ''observed proportion''. To obtain a null distribution, we performed 1,000 permutations where, for each iteration, we: i) sampled the same number of genes as DE genes in our set (146 for WT and 169 for *CypD*$^{-/-}$) from a list of all genes tested, and ii) calculated the proportion of these genes that are also in the TiRe gene set (our ''null percentage''). p-values were computed by evaluating the number of permutations in which the null percentage was greater than or equal to the observed percentage divided by the number of total permutations (n = 1,000).